Real Schur Flows

Jian-Zhou Zhu(朱建州)*

Su-Cheng Centre for Fundamental and Interdisciplinary Sciences,

Nanjing 211316, China

Abstract

The problem of a flow with its velocity gradient being of *real Schur form* uniformly in a cyclic box is formulated for numerical simulation, and a semi-analytic algorithm is developed from the precise structures. Computations starting from two-component-two-dimensional-coupled-with-one-component-three-dimensional initial velocity fields of the Taylor-Green and Arnold-Beltrami-Childress fashions are carried out, and some discussions related to turbulence are offered for the multi-scale eddies which, though, present precise order and symmetry. Plenty of color pictures of patterns of these completely new flows are presented for general and specific conceptions.

Keywords: computational real Schur fluid mechanics, rotating flow, passive scalar

* jz@sccfis.org

I. INTRODUCTION

As shown in Fig. 1 for a prototypical flow of the Taylor-Green [1] fashion described by Eq. (20) below, a two-component-two-dimensional coupled with one-component-three-dimensional (2C2Dcw1C3D) velocity field, with the 'horizontal' components, u_1 and u_2, presenting columnar/two-dimensional (2D) patterns and the 'vertical' component u_3 fully three-dimensional (3D) one, has the velocity gradient uniformly of the real Schur form, thus a *real Schur flow* (RSF). Such RSF is of interesting mathematical value and physical relevance ([2] and references therein). A better understanding of how such anisotropic structure is maintained dynamically may also shed light onto the opposite problem of isotropization in Navier-Stokes flows (NSF), which is of course fundamentally important, especially for turbulence. However, RSF, formally simplifying, say, the full Navier-Stokes flow (NSF), can still be very complicated, welcoming also systematic numerical investigations to explore it in detail. Actually, as we shall see, finding and designing algorithms for computing RSF by itself requires in-depth investigation of the dynamics, especially the fine structures.

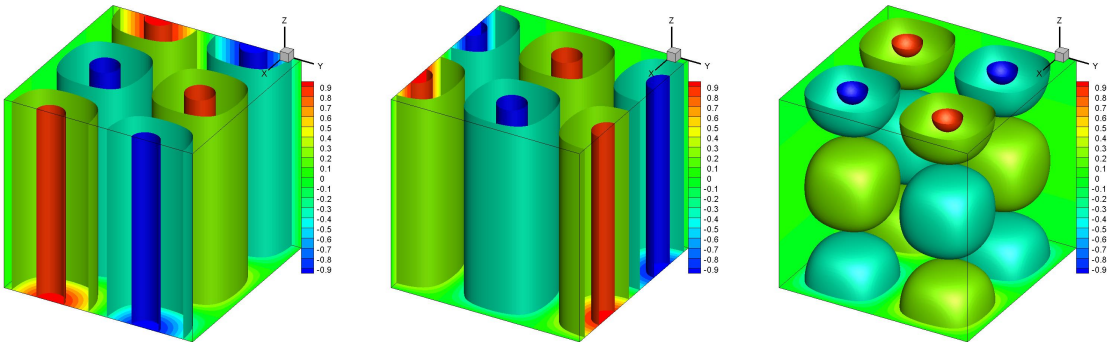

FIG. 1: The isosurfaces (of values ± 0.9 and ± 0.3) of the three components, u_1 (left), u_2 (middle) and u_3 (right), of the Taylor-Green-fashion 2C2Dcw1C3D velocity field.

Note that an RSF in the natural Navier-Stokes setting is of course unstable, but extra physical constraint, such as strong rotation or background magnetic field, among others, may stabilize it. Thus, singling it out for separate study makes a lot of sense.

Numerical computation of RSF is nontrivial in the sense that the above defining property of the velocity does not directly specify the precise and complete form of the governing equation(s) appropriate for discretization and integration. Mathematically speaking, RSF lives in a subset of the (phase) space of NSF, requiring appropriate constraint(s) to avoid

escaping. In other words, dynamically, a set of additional precise relations should be satisfied to have a self-consistent evolution of the system. Under the framework of NSF, it has been shown that such relations can be explicitly written down, in the sense of particular properties of the (primitive) variable itself as a function of space and time, for the inviscid case or for the slightly simplified viscosity model with, say, the dilatational effect neglected in the Stokesian model [2]. This makes it possible to define a dynamical projection operator straightforward for numerical implementation. For the more general cases, including models such as non-newtonian fluid or quantum NSF, the precise structures are typically not explicitly expressible but implicity specified, in the sense of some particular relation(s) between different (primitive) variables. It is possible that one may make use of (some of) the precise relations to apply in a 'brute-force' way the conventional dual-time stepping method [3] with the inner iterations (pseudo-time) for the accurate relaxation to the self-consistent state before advancing the physical time. How to ensure the convergence of the inner iteration and how accurate or how many (pseudo-time) steps are needed for the self-consistent RSF dynamics are in general not easy to be made clear and can be subtle. Another brute force is to resort to approaches related to molecular dynamics. For example, Gallis et al. [4] recently made a comparison between the direct simulation Monte Carlo (DSMC) and direct numerical simulation (DNS) of the compressible continuum model for the evolution starting from the Taylor-Green field (TGF [1]). For RSF, however, specific rules at the micro- or meso-scopic level need to be found and implemented in the computation, which, among other issues such as the (virtual) molecule number and noise of DSMC as addressed in Ref. [4] (see also the discussions of simulations of incompressible TGF evolution by discrete unified gas-kinetic scheme, pseudo-spectral and lattice Boltzmann methods [5]), again is not obvious. Both such types of algorithms are interesting and probably challenging, and, definitely deserve to be pursued. Here, as a first step, we discuss a semi-analytical algorithm, for DNS of RSF, based on the evolution equation dynamically projected from the full Navier-Stokes with the explicit analytical expressions for the precise relations.

For physical interest, RSF has been suggested to be possibily playing the role in general turbulence dynamics as special relativity in general relativity and, particularly, the helical RSF were proposed to be the 'chiral base flow (CBF)' for understanding the helicity effect on the compressibility of flows of neutral and ionized gases [6]. It is thus natural to numerically examine the very basic issues such as the production of small RSF eddies, a praradigm with

TGF [1, 7, 8] extended also to different numerical concerns of compressible flows [9, 10], and to test the relevant resutls in Ref. [6], such as the 'fastening' (compressibility-reduction) effect of helicity (compared to achiral base flow — aCBF).

In Sec. II, we formulate RSF equations for numerical simulation, and, design the algorithm and solution strategy. In particular, Eqs. (1a and 1b+), together with Eqs. (1b- and 1c), are established to compute isothermal RSF in a cyclic box with the semi-analytical algorithm. In Sec. III, the specific physical problem and numerical method, with Eq. (1b) alternative to Eqs. (1b- and 1b+), are presented, which is followed by Sec. IV for the discussion of the results, especially the production and properties of small RSF eddies. Sec. V concludes the work with further discussions.

II. FORMULATION AND ALGORITHM

A. Starting from NSF

Let's start with the Euler equation in $\mathbb{E}^3$ for the RSF with (nondimensional) density ρ, pressure p, velocity $\boldsymbol{u}$,

$$\partial_t \rho = -\nabla \cdot (\rho \boldsymbol{u}) =: {}^0RHS, \tag{1}$$

$$\partial_t \boldsymbol{u}_h = -\boldsymbol{u}_h \cdot \nabla_h \boldsymbol{u}_h - \rho^{-1} \nabla_h p =: {}^h\boldsymbol{rhs}, \tag{1b-}$$

$$\partial_t u_3 = -(\boldsymbol{u}_h \cdot \nabla_h u_3 + u_3 u_{3,3}) - \rho^{-1} p_{,3} =: {}^3rhs, \tag{1c}$$

where x_1 and x_2 are the '$_h$orizontal' coordinates and the corresponding $\boldsymbol{u}_h := \{u_1, u_2\}$ is independent of the 'vertical' coordinate x_3, i.e.,

$$\boldsymbol{u}_{h,3} \equiv 0. \tag{2}$$

For the barotropic case,

$$(\nabla p)/\rho = \nabla \Pi \tag{3}$$

where Π is the specific enthalpy, and the isothermal (constant-temperature) relation $p = c^2 \rho$ results in

$$\nabla \Pi = c^2 \nabla \ln \rho, \tag{4}$$

where c is the sound speed. Internal viscosity (resp., external acceleration) models of $\boldsymbol{M}_h$ and M_3 (resp., $\boldsymbol{a}_h$ and a_3) can be added to (1b- and 1c) respectively, and our objective is

then to find the numerical solutions of Eqs. (1, 1b- and 1c) constrained by Eq. (2), which in general requires appropirately designed algorithms for performing consistent computations to obtain the accurate results. In this note, we are not interested in very complicated situations or sophisticated computations, but would rather look for reasonable simplications and semi-analytical treatments to compute RSF.

The viscosity model $\boldsymbol{M}(\boldsymbol{u})$ is determined by the constitutive relation of the medium. For the (generalized) Newtonian fluid, there is a dilational or 'second viscosity' coefficient whose neglection leads to the Stokesian model (thus the Navier-Stokes)

$$\boldsymbol{M}(\boldsymbol{u}) = \mu\rho^{-1}\nabla^2\boldsymbol{u} + \frac{\mu}{3\rho}\nabla(\nabla\cdot\boldsymbol{u}) \tag{5}$$

when the dynamical viscosity μ is constant. For simplicity, we will focus on the model $\boldsymbol{M}(\boldsymbol{u}) = \nu\nabla^2\boldsymbol{u}$ applied in incompressible flows with constant kinetic viscosity ν. This is not always very realistic, but can be a good approximation in many physical situations, unless the flow is extremely compressible with very high tempearture, say. In such a case,

$$\boldsymbol{M}_h = \nu\nabla_h^2\boldsymbol{u}_h, \text{ and } M_3 = \nu\nabla^2 u_3. \tag{6}$$

Note that for analytical (e.g., Ref. [11] and recently [2]) and/or numerical (e.g., Refs. [12, 13]) convenience, Eq. (1) has also been written for the 'logarithmic variable', $\ln\rho$,

$$\partial_t \ln\rho = -\boldsymbol{u}\cdot\nabla\ln\rho - \nabla\cdot\boldsymbol{u}, \tag{7}$$

which is equivalent except for the vacuum solution that we are not interested in here.

On the other hand, particularly for the computational fluid dynamics (CFD) formulation and programming, and, for better behavior of shock-capturing schemes (e.g., Ref. [14]), it is also useful to write in the following *conservative form* for the Navier–Stokes equations of the compressible flow of an ideal gas

$$\begin{cases} \boldsymbol{U}_{,t} = -\boldsymbol{F}_{j,j} + \boldsymbol{V}_{j,j} =: \boldsymbol{RHS}, \\ p = \rho\mathcal{R}T, \end{cases} \tag{8}$$

where

$$\boldsymbol{U} = \begin{pmatrix} \rho \\ {}^h\boldsymbol{U} \\ \rho u_3 \\ E \end{pmatrix}, \quad \boldsymbol{F}_j = \begin{pmatrix} \rho u_j \\ \rho u_1 u_j + p\delta_{1j} \\ \rho u_2 u_j + p\delta_{2j} \\ \rho u_3 u_j + p\delta_{3j} \\ (E+p)u_j \end{pmatrix}, \quad \boldsymbol{V}_j = \begin{pmatrix} 0 \\ \sigma_{1j} \\ \sigma_{2j} \\ \sigma_{3j} \\ \sigma_{jk}u_k + \kappa T_{,j} \end{pmatrix}, \tag{9}$$

with ${}^0U := \rho$ and ${}^h\boldsymbol{U} := \begin{pmatrix} \rho u_1 \\ \rho u_2 \end{pmatrix}$ to which correspond the ${}^0RHS$ and ${}^h\boldsymbol{RHS}$ (for later reference), respectively, in $\boldsymbol{RHS}$. Here, δ_{ij} is the Kronecker delta, and the summation over repeated indices has been assumed; κ is the conductivity of the temperature T, and $\mathcal{R}$ is the ideal gas constant. The total energy is $E = \frac{p}{\gamma-1} + \frac{1}{2}\rho u_j u_j$ where $\gamma \equiv C_p/C_v$ is the adiabatic exponent, the ratio of the constant-pressure heat capacity C_p to the constant-volume one, C_v. The viscous stress $\sigma_{ij} = \mu\left(u_{i,j} + u_{j,i}\right) - \frac{2}{3}\mu\theta\delta_{ij}$, in general also accounts for the dilatation $\theta := \nabla \cdot \boldsymbol{u}$. The dynamic viscosity μ assumes Sutherland's law [15] $\mu = \frac{1.4042T^{1.5}}{T+0.40417}\mu_\infty$ with $\mu_\infty = 1.716 \times 10^{-5}$kg/(m·s): μ is indeed constant when T is not varying (isothermal), which is a good approximation for moderate cases free of boundary.

B. The governing equations for RSF

The RSF has not only the defining characteristics in the velocity but also some particular thermodynamic structures which govern the dynamics. Below, we will derive the results from the 2C2Dcw1C3D velocity field for the 3-space dynamics (more complete analytical results, including those for high-dimensional space and Lie invariances, are discussed in another note [2]).

Taking derivative with respect to x_3 in Eq. (1b-) for the horizontal momentum, Eq. (2) indicates [16]

$$[(\nabla_h p)/\rho]_{,3} = 0 \tag{10}$$

by the requirement of RSF uniformly over space and time, which leads to nontrivial consequence as follows.

By Eq. (3), the barotropic Eq. (10) writes

$$(\nabla_h \Pi)_{,3} = 0 \text{ (or } \Pi_{,13} = \Pi_{,23} = 0), \tag{11}$$

which simply means, in words, Π should be decomposed into two functions, $\mathscr{P}_h$ and $\mathscr{P}_3$, one of only the horizontal coordinate $\boldsymbol{x}_h := \{x_1, x_2\}$ and the other of only x_3. To be precise, Eq. (11) means $\boldsymbol{F}_h(\boldsymbol{x}_h) := \nabla_h \Pi$ is a (vector) function of only the horizontal coordinate $\boldsymbol{x}_h$ and $F_3(x_3) := \Pi_{,3}$ a function of only x_3, which leads to

$$\Pi = \mathscr{P}_3(x_3) + \mathscr{P}_h(x_1, x_2) \tag{12}$$

where

$$\mathscr{P}_h := \int\int \boldsymbol{F}_h \cdot d^2\boldsymbol{x}_h \Big|^h \text{ and } \mathscr{P}_3 := \int F_3 dx_3 \Big|^3, \tag{13}$$

with $\Big|^h$ meaning "ignoring the x_3-dependent integration constant which is absorbed by $\mathscr{P}_3$" and $\Big|^3$ "ignoring the $\boldsymbol{x}_h$-dependent integration constant which is absorbed by $\mathscr{P}_h$".

We may consider the RSF in a box of dimension $L_z \times L_2 \times L_3$, cyclic in each direction, or with $L \to \infty$ in some direction(s) with the field vanishing sufficiently fast. Introducing

$$\langle\bullet\rangle_{12} := \frac{\int_0^{L_2}\int_0^{L_1} \bullet dx_1 dx_2}{L_1 L_2},\ \langle\bullet\rangle_3 := \frac{\int_0^{L_3} \bullet dx_3}{L_3} \text{ and } \langle\bullet\rangle_{123} := \frac{\int_0^{L_1}\int_0^{L_2}\int_0^{L_3} \bullet dx_1 dx_2 dx_3}{L_1 L_2 L_3}, \tag{14}$$

we have

$$\langle\Pi\rangle_3 = \mathscr{P}_h(x_1, x_2) + \langle\mathscr{P}_3\rangle_3, \tag{15a}$$

$$\langle\Pi\rangle_{12} = \mathscr{P}_3(x_3) + \langle\mathscr{P}_h\rangle_{12}, \tag{15b}$$

$$\langle\Pi\rangle_{123} = \langle\mathscr{P}_h\rangle_{12} + \langle\mathscr{P}_3\rangle_3 = \langle\Pi\rangle_{12} + \langle\Pi\rangle_3 - \Pi,$$

$$\text{i.e., } \Pi = \langle\Pi\rangle_{12} + \langle\Pi\rangle_3 - \langle\Pi\rangle_{123}. \tag{15c}$$

Rewriting Eq. (1) or (7) as

$$\partial_t \ln\rho = -\boldsymbol{u}\cdot\nabla\ln\rho - \nabla\cdot\boldsymbol{u} = {}^0\!RHS/\rho =: {}^0\!\mathscr{rhs} \tag{16}$$

and taking, with Eq. (4) for the isothermal case, the specific enthalpy particularly (ignoring the irrelevant constant)

$$\Pi = c^2 \ln\rho = c^2(\langle\ln\rho\rangle_{12} + \langle\ln\rho\rangle_3 - \langle\ln\rho\rangle_{123}), \tag{17}$$

and, by bringing Eqs. (17 and 15c) into Eq. (16) with the interchangeability of the order of the time derivative and the average operators defined in Eq. (14) and with

$$\langle u_{1,1}\rangle_1 = \langle u_{2,2}\rangle_2 = \langle u_{3,3}\rangle_3 = 0 \tag{18}$$

from the periodic boundary condition, we finally obtain the partial-integral-differential equation (not the original conventional partial differential equation — PDE)

$$\partial_t \ln\rho = \langle {}^0\!\mathscr{rhs}\rangle_{12} + \langle {}^0\!\mathscr{rhs}\rangle_3 - \langle {}^0\!\mathscr{rhs}\rangle_{123} \tag{1a}$$

It is seen that the above derivation works also for the case with a 2C2Dcw1C3D external acceleration ('force' divided by the mass per volume in Newtonian mechanics) $\boldsymbol{a}$ applied to Eqs. (1b- and/or 1c), with the horizontal component $\boldsymbol{a}_h$ being independent of x_3.

Eq. (1a) summarizes Eqs. (1, 2 and 10) and, together with Eqs. (1b- and 1c), completely defines the dynamics of the 2C2Dcw1C3D isothermal flow in a cyclic box, even for the driven case with 2C2Dcw1C3D acceleration added, as just mentioned.

Actually, Eq. (1a) applies in more general nonbarotropic RSFs which present other precise structures as well [2] (c.f., the winding-up discussion in Sec. V), but we focus only on the isothermal case in this note for the (numerical) proof of concept.

C. The strategy and algorithm for simulations

We focus on the isothermal RSFs in a cyclic box of dimension $2\pi \times 2\pi \times 2\pi$. Our algorithm for integrating our partial-ingral-differential equations can be developed from the standard method of CFD. As can be seen from the governing equations, particularly (1a), of RSF dynamics established in the above, *the first part* involves the familiar discretization and computation of the compressible Navier-Stokes quation, in which, as mentioned, the wisdom is that the conservative Eq. (8), where Eq. (1), instead of (1a), is appropriate for use in the case of high speed flows with shocks needed to be captured accurately [14]: Eqs. (16 and 1a) are not in the conservative form. The latter can be directly used for discretizing and integrating weakly compressible flows [13] but in general do not quite satisfy our interests of the flows also involving (strong) shocks. So, we need a combination of the two methodologies, both appear to be most conveniently realized by the mature high-order finite difference schemes, such as the compact and weighted essentially non-oscillator (WENO) schemes [17] used in various relevant studies [18–21].

Our strategy is to compute Eqs. (16 and 1a) in an actually-conservative way, in the sense that the ${}^0\mathcal{RHS}$ of Eq. (16) is computed from the ${}^0RHS$ of Eq. (1), simply by $(\ln\rho)_{,t} = \rho_{,t}/\rho$. $\boldsymbol{u}$ can also be used as the primitive variable but integrated in such an actually-convervative method (see below). Since the transformation (dividing by ρ) involves only the local variable without derivative and ρ is nonvanishing (we won't study the problem with vacuum in this note, as said), neither accuracy loss nor singular issue will arise.

With such a strategy, *the second part* then can be performed, after the (actually-conservative) fluxes are computed, with the spatial averaging operators defined in Eq. (14). Higher-order time accuracy, such as the Runge-Kutta methods, then can be applied for (explicit) time marching, completing the implemention of a semi-analytical algorithm.

We remark that in principle Eqs. (1a, 1b- and 1c) completely defines the 2C2Dcw1C3D flow without the necessity of imposing other precise analytical relations derived in the last section. However, due to numerical errors in computing $\boldsymbol{u}_h$ with Eq. (1b-) or obtaining $\boldsymbol{u}_h$ through $\boldsymbol{u}_h = \rho\boldsymbol{u}_h/\rho$ from the computation of the conservative Eq. (8), i.e., the second and third components of (8 and 9), it is practically needed to impose, say, Eq. (2) which reads in terms of computation

$$\boldsymbol{u}_h = \langle \boldsymbol{u}_h \rangle_3, . \tag{1b+}$$

We will come back to this point in Sec. III B.

III. THE PHYSICAL PROBLEM AND NUMERICAL METHODS

As said in the introductory discussions, the local structure of a general flow is of RSF up to an $O(3)$ transformation of the coordinates in the neighborhood of a point, which is at the second-order accuracy with respect to the size of the local domain, because the velocity gradient involves the first-order spatial derivatives of the velocity. This is very much resembling the situation in the classical general relativity concerning the local inertial frame in which a (strong) equivalence principle is introduced. What's more, the formal fast-rotating limit, i.e., the compressible Taylor-Proudman theorem, corresponds to an RSF. Thus, it appears that there is every reason to explore fundamental problems of such flows. Indeed, it is speculated in Ref. [6] that the knowledge of RSF may provide the basis of the 'strong equivalence principle' to describe the general turbulence. Thus, systematic and extensive numerical investigations of RSF, turbulence or not, are promising, which requires a proof of concept with definite physical problem and numerical solution, as is the purpose of this section.

A most fundamental problem in fluid turbulence is the development of multi-scale structures and small-scale dissipation, associated to the singularities (complex or real). A paradigm has been studying the evolution of the so-called Taylor-Green field (TGF) [1] and Orszag-Tang field (OTF) [22]. Indeed, much further has been carried forward along this way for incompressible (e.g., Refs. [7] and [23], respectively for TGF and OTF) and also compressible flows, for the latter of which it has even been proposed as the 'benchmark' case for numerical methods (e.g., Ref. [9] and [24], respectively for TGF and OTF). The OTF studies have been also carried out in 3D magnetohydrodynamics (MHD) (e.g., Refs. [25]).

Actually, though our studies may be extended to plasma flows [6], we shall restrict ourselves in the neutral gas. And, corresponding to OTF, actually, as we shall see, it appears more precise to consider the Arnold-Beltrami-Childress flow (ABCF: [26]).

We will freely apply the correpondences $x \leftrightarrow x_1$, $y \leftrightarrow x_2$ and $z \leftrightarrow x_3$ for historical reason associated to TGF and ABCF, and $\boldsymbol{\omega}$ denotes the vorticity of the velocity field.

A. The physical problems

The TGF (after appropriate normalizations and reparameterization with a rotation angle θ [7]) and ABCF read, respectively,

$$ {}^{TGF}\boldsymbol{u} = \begin{pmatrix} \frac{\sin(\theta+2\pi/3)}{\sqrt{3}} \sin x \cos y \cos z \\ \frac{\sin(\theta-2\pi/3)}{\sqrt{3}} \cos x \sin y \cos z \\ \frac{\sin\theta}{\sqrt{3}} \cos x \cos y \sin z \end{pmatrix}, \quad {}^{ABCF}\boldsymbol{u} = \begin{pmatrix} A\sin z + B\cos y \\ C\sin x + A\cos z \\ B\sin y + C\cos x \end{pmatrix}, \tag{19} $$

where OTF (with an extra u_z component) corresponds to $A = 0$, $B = 1$ (with y replaced by $y + \pi/2$) and $C = 1$.

Before proceeding, it is better putting some terminologies in to the following

Definition 1 *A vector field $\boldsymbol{v}$ is 'purely helical' if each of the Fourier component $\hat{\boldsymbol{v}}(\boldsymbol{k}) = \int\int\int \boldsymbol{v} \exp\{-\hat{i}\boldsymbol{x}\cdot\boldsymbol{v}\} d^3\boldsymbol{x}$ is a 'helical mode', the latter meaning that $\hat{i}\boldsymbol{k}\times\hat{\boldsymbol{v}} = \pm k\hat{\boldsymbol{v}}$ with $\hat{i}^2 = -1$. The $+$ and $-$ signs are usually asigned respectively to right- and left-handnesses. And, $\boldsymbol{v}$ is 'Beltrami' if $\exists\kappa,\ \kappa^2 > 0,\ \nabla\times\boldsymbol{v} = \kappa\boldsymbol{v}$.*

The local helicity density of TGF vanishes everywhere, ${}^{TGF}\boldsymbol{\omega}\cdot\ {}^{TGF}\boldsymbol{u} = 0$, while ABCF is purely helical, actually 'Beltrami'[26].

We first remark that the approximate analytical calculations similar to that of Taylor and Green [1] is formidable, if possible to any degree, for the compressible case, because the density modes enter and the pressure can not simply be determined by the Poisson equation, even if initially is. For our RSFs, with the additional precise structures obtainable (see also Ref. [2] for more), the problem might be more tractable, but definitely nontrivial, and the numerical studies are highly desirable.

1. *2C2Dcw1C3D*

We first consider the TGF fashion RSF velocity

$$\boldsymbol{u} = \begin{pmatrix} \cos x \sin y \\ -\sin x \cos y \\ \sin x \sin y \cos z \end{pmatrix}. \tag{20}$$

It appears in Fig. 2 for the field pattern that the isosurfaces of small-amplitide vorticity are highly three dimensional while those of high amplitude are only weakly depending on z.

$\boldsymbol{u}$ is already fully 2C2Dcw1C3D, thus the simplest initial density can just be uniform $\rho(t_0) = 1$. We can of course also compute from the isothermal relation the one corresponding to which the pressure gradient balances the 'parallel' (to wavevector) component of the nonlinear advection term, as is usually done in TGF-relevant studies: such balance however, unlike in the incompressible flow, is not prereserved, thus no obvious reason for such a choice in our study. The different initial pressure/density fields will lead to different relaxation at the very beginning and probably much later on, here we however shall not digress into such studies but only focus on issues related to the proof of concept, such as the differences between two viscosity models, one being of the incompressible flow, while the other being Stokesian with the dilatation effect (but without the 'second viscosity').

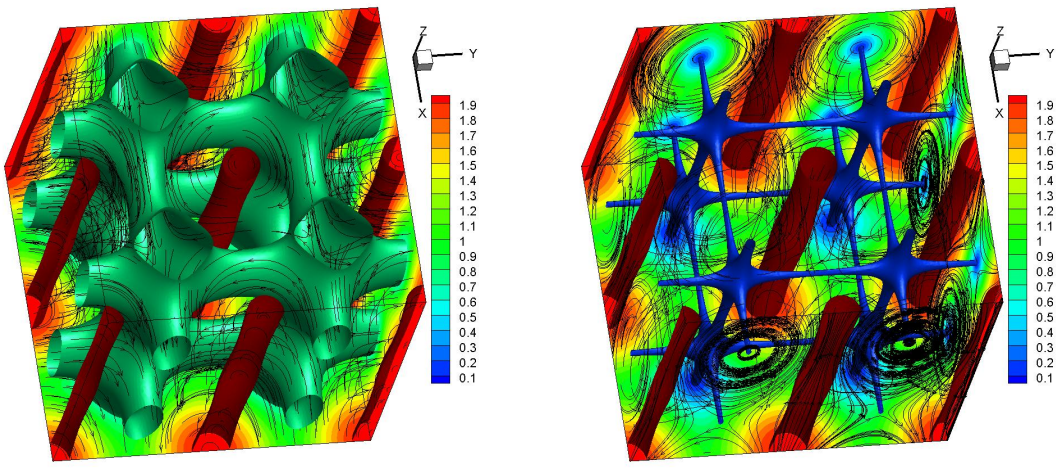

FIG. 2: The vorticity strength slices and isosurfaces (0.7 and 1.9 in the left panel, and, 0.1 and 1.9 in the right one), and, velocity (left) and vorticity (right) streamlines.

Nevertheless, the problem of flow compressibility difference between CBF and aCBF remarked in the introductory discussions should not be neglected, thus comes the issue of 'fair comparison': when we have CBF and aCBF with the same transversal and parallel (to wavevector) energies, and, the same density field, among others, the initial acceleration fields (or the 'impulses') are different, and vise versa. Thus, absolutely 'fair' comparison is in general impossible, and what can be pursued is to be essentially fair in exposing the different physical consequences. We will come back to this point in Sec. III A 2 for the fields related to the following helical decomposition.

The local helicity density $\boldsymbol{\omega}\cdot\boldsymbol{u}=0$ for $\boldsymbol{u}$ in Eq. (20). We then can compute the purely helical, say, the right-handed ${}^R\boldsymbol{u}$ from the standard helical decomposition of the Fourier coefficients ([27, 28]: explicit formula given in Sec. III A 2), but, unfortunately, such ${}^R\boldsymbol{u}$ is not an RSF. It is of course easy to design helical but not purely helical RSFs, with the freedom of u_z with z dependence. For purely helical RSF, we have to turn to the field independent of the vertical coordinate z, that is a three-component-two-dimensional (3C2D) velocity, due to the following

Theorem 1 *A 2C2Dcw1C3D but not 3C2D flow can not be 'purely helical'.*

Proof. $\boldsymbol{u}_{h,3}=0$ means $\hat{u}_1(\boldsymbol{k})=\hat{u}_2(\boldsymbol{k})=0\ \forall\ k_3\neq 0$. The helical, say, without loss of generality, the right-handed Fourier mode $\hat{\boldsymbol{u}}_h$, satisfies however, e.g., $\hat{i}(k_1\hat{u}_2-k_2\hat{u}_1)=k\hat{u}_3$ by definition 1, and contradiction results if $k_3\hat{u}_3(\boldsymbol{k})\neq 0$ for $k_3\neq 0$. □

In other words, a purely helical 2C2Dcw1C3D flow must be 3C2D which satisfies our purpose here. And, ABCF in Eq. (19) with $A=0$ but $BC\neq 0$ is purely helical 3C2D RSF.

2. 3C2D

To have a comparison between purely neutral (with right- and left-handed sectors exactly balanced) and purely helical RSF initial fields, we then consider

$$\boldsymbol{u}=\begin{pmatrix}\cos x\sin y\\ -\sin x\cos y\\ \sin x\sin y\end{pmatrix},\quad {}^R\boldsymbol{u}=\begin{pmatrix}\frac{1}{2}\left(\sqrt{2}\cos x\sin y+\sin x\cos y\right)\\ \frac{1}{2}\left(-\sqrt{2}\sin x\cos y-\cos x\sin y\right)\\ \frac{1}{2}\left(\sqrt{2}\sin x\sin y-2\cos x\cos y\right)\end{pmatrix}. \tag{21}$$

In the above, ${}^R\boldsymbol{u}$ is computed from the helical decomposition of Fourier coefficients [27, 28],

$${}^R\hat{\boldsymbol{u}}=(\hat{\boldsymbol{u}}+\hat{i}\boldsymbol{k}\times\hat{\boldsymbol{u}}/k)/\sqrt{2}, \tag{22}$$

of the incompressible $\boldsymbol{u}$, representing the purely right-handed helical sector. The reason we do this is because, just like TGF, here $(\nabla \times \boldsymbol{u}) \cdot \boldsymbol{u} = 0$. We will compare the evolutions from such fields, both augmented with, say,

$$\rho(t_0) = \rho_0(1 + \epsilon \cos z) \tag{23}$$

where ρ_0 (= 1 here) is the reference density and $1 > |\epsilon| \neq 0$. The pressure $p = c^2\rho$ then will drive the isothermal flow to be 2C2Dcw1C3D during which small eddies are produced.

Both velocities are incompressible and $\int_0^{2\pi}\int_0^{2\pi} \boldsymbol{u}^2\, dxdy = \int_0^{2\pi}\int_0^{2\pi} {}^R\boldsymbol{u}^2\, dxdy$, for which, in Eq. (22), we have particularly replaced the factor 1/2 in the stardard formular [27, 28] with $1/\sqrt{2}$. However, the two chiral sectors of vorticities of $\boldsymbol{u}$ can cancel, leading to much smaller minimum (≈ 0) of $|\nabla \times \boldsymbol{u}|$ than that of the purely helical sector (≈ 1.4), while the maxima of the former (2.0) is larger (due to mutual enhancement) than the latter (≈ 1.0, in Fig. 3), which already indicates the insufficiency or incompleteness of the traditional terminology in compressible or aeroacoustic turbulence context [11] of 'vortical' or 'shear' mode (compared to the dilational/compressive mode, c.f., Ref. [32] and references therein). Fig. 3 compares the vorticity strength and velocity streamlines of the two initial fields, showing the different flow patterns, though the vorticity strength patterns look similar (with strong quantitative distinction). Also presented in the right pannel is the computed helicity density and the vorticity-streamline pattern: it looks the same as the middle panel, because ${}^R\boldsymbol{u}$ is a Baltrami field due to the fact that the two modes of $\boldsymbol{u}$ has the same wavelength $k = \sqrt{2}$. For more details, this Beltrami field satisfies $\nabla \times \boldsymbol{u} = k\boldsymbol{u}$, and actually, corresponding to the maximum and minimum figures of vorticity amplitudes given in the above, the maximum of helicty is indeed $1.41^2/\sqrt{2} \approx 1.41$ while the minimum, again indeed, $(1.0)^2/\sqrt{2} \approx 0.71$ [the maxima and minima given the legends for contours are in general close to but not exactly the actual ones]. In other words, we already have the OTF- or ABC-fashion initial field given in the second half of Eq. (19) to which only a variable tranformation is needed from the second half of Eq. (21).

The above set up of CBF and aCBF appear to be good for comparing the evolution of compressibility. The initial acceleration fields and the changing rates of velocity divergence are in general different, from the beginning to the end (when 'everything' is transformed into thermal motions by viscosity), resulting in the physical conclusions in Sec. IV B consistent with the 'fastening' notion [6]. In other words, it is, in a sense, appropriate to conclude

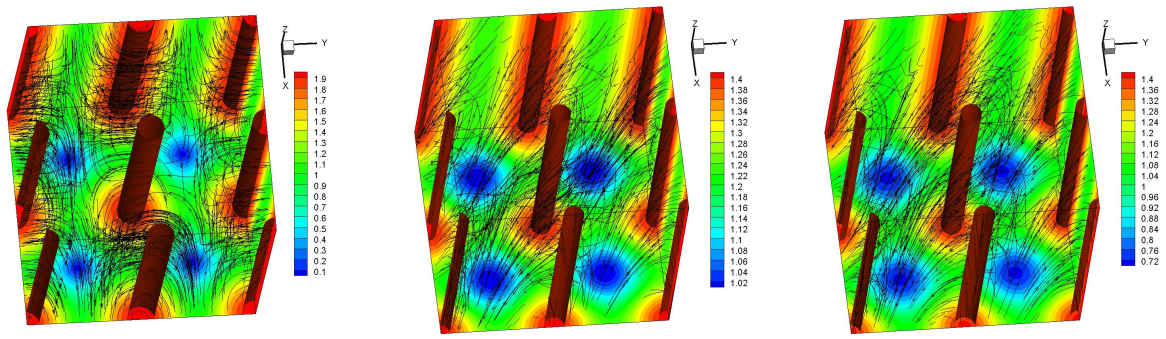

FIG. 3: The vorticity strength ($|\nabla \times \boldsymbol{u}|$) slices and isosurfaces and, velocity streamlines of $\boldsymbol{u}$ (left) and ${}^{R}\boldsymbol{u}$ (middle), the slices, isosurfaces, helicity density and vorticity streamlines of the latter is also presented in the right pannel (exactly the same/isomorphic to the middle pannel due to the Beltramity).

the 'unfair/different' consequences from essentially fair physical conditions for dynamical analysis. Similarly is the situation with random initial fields and/or forcing, in which case it is obvious impossible to have many details to be the same, except for the relevant statistics, for an essentially fair comparison of turbulence. Detailed discussions of the latter however belong to another communication.

B. Numerical method

As remarked in the end of Sec. II C, the problems in Sec. III A with initial data of RSF should be solved with the equations established there. However, though the problem and mathematical description are already complete, the standard CFD procedure and the RSF-specialization, such as the extra imposition of Eq. (2), actually contain important technical details in the numerical method and need further clarification.

1. The standard CFD part

In the numerical implementation, the first part, as mentioned in Sec. II C, for our purpose can in principle any suitable standard CFD method, in the prodecure of which Eq. (8) is normalized by the characteristic length ℓ^*, velocity u^*, time L/U, density ρ^*, temperature T^*, pressure $\rho^*\mathcal{R}T^*$, kinetic energy ρ^*U^2, sound speed $c^* = \sqrt{\gamma\mathcal{R}T^*}$, dynamic viscosity μ^*, and

heat conductivity coefficient κ^*. The normalization results in non-dimensional parameters, including the Reynolds number $Re := \rho^* UL/\mu^*$, Mach number $Ma := U/c^*$, Prandtl number $Pr := \mu^* C_p/\kappa^*$, and adiabatic exponent of gas γ, and total energy now reads

$$E = \frac{p}{(\gamma - 1)\gamma Ma^2} + \frac{1}{2}\rho u_j u_j. \tag{24}$$

Our isothermal case simply corresponds to that with unit value of T. We solved the nondimensionalized equation with various initial parameters with, for instance, the Mach number Ma ranging from 0.1 to 2.0 for various tests and checks, but here only the simulations in a cube of dimension 2π resolved with 128^3 uniform grids for $\gamma = 1.4$, $Pr = 0.7$, $Re = 450$ and $Ma = 1$ are reported, as the proof of concept. More detailed and specific studies of (complex) singularities, fully developed turbulence with random structures, among others which may require higher resolution and precision, and, even other approaches such as the pseudo-spectral method [29], are beyond the scope of this communication.

In the RSF solver for these specific computations, assembling of the conservation and nonconservation forms of the Navier–Stokes equation has been made. In particular, the equation for the logarithmic of density for time marching with its right-hand side however is computed from the method using the conservative form in terms of density itself. Using the logarithmic of density is a must for RSF as already indicated earlier and will be further explained below, while using the conservative form for discretization is to capture the shocks well [14]. Specifically for the finite-difference schemes, the viscous terms are discretized by the compact eighth-order finite difference scheme and the convective terms are discretized by the seventh-order weighted essentially non-oscillatory (WENO) schemes [20, 21]. The time integration is advanced by the third–order total variation diminishing Runge-–Kutta method [30].

2. The second RSF-specialization part

Some more important details of the second RSF-specialization part follow: with

$$^h\boldsymbol{RHS} = (\rho \boldsymbol{u}_h)_{,t} = \rho \boldsymbol{u}_{h,t} + \rho_t \boldsymbol{u}_h = \rho \; ^h\boldsymbol{rhs} \; + \; ^0\!rhs \; \boldsymbol{u}_h \tag{25}$$

and $^0\!rhs \; = \; ^0\!RHS/\rho$ defined in Eq. (16), we have

$$\boldsymbol{u}_{h,t} = \; ^h\boldsymbol{rhs} = \left[^h\boldsymbol{RHS} \; - \; \boldsymbol{u}_h \; ^0\!RHS/\rho \right] /\rho. \tag{26}$$

Given Eqs. (1a and 1b-) and the initial RSF data, the RSF evolution is mathematically assured, however, with ${}^h\boldsymbol{RHS}$, ${}^0RHS$ and ρ containing the z-dependence not numerically cleanly removed as in Eq. (1a), the computation of ${}^h\boldsymbol{rhs}$ in Eq. (26) needs clearing up the z-dependent errors. Thus, according to Eq. (1b+) and the interchangeability of the order of time derivative and spatial averaging, we should in stead compute

$$\boldsymbol{u}_{h,t} = \langle (\rho\ {}^h\boldsymbol{RHS}\ -\ {}^0RHS\ \boldsymbol{u}_h)/\rho^2 \rangle_3. \tag{1b}$$

That is, the 'numerically complete' governing equations are (1a,1b and 1c), and solving such a system with whatever numerical discretization scheme may be considered as the 'semi-analytical' method, in the sense that the $\boldsymbol{u}_{h,3} \equiv 0$ property is automatically satisfied by the self-consistent dynamical equations and the errors from whatever numerical discretizations and integrations in this repspect is cleanly removed, up to the computer roundoff. Since it is purely the purpose of removing the numerical errors to perform (*i*) the computation of Eq. (1b), i.e., additional spatial averages over Eq. (26) and (*ii*) that imposing Eq. (1b+) after computing $\boldsymbol{u}_h$ from ${}^h\boldsymbol{U}$ in Eq. (8) mentioned in the end of Sec. II C, there should be no difference between the latter two approaches, as indeed verified by numerical tests. For the current purpose of the problems set up in Sec. III A, the computation of (*ii*) is actually more economy, with less spacial averaging or Fourier mode truncation.

Simply imposing the extra Eq. (1b+) in each step of solving the original, say, the conservative-form Eq. (8), in the standard CFD may not be considered as completely 'wrong' but should be regarded only a 'primitive' or 'zeroth order' scheme (which is possible to be improved with other techniques such as the dual-time stepping method [3]). Such a 'naive' treatment does not take the self-consistent RSF dynamics with the accompanying precise structures in Sec. II B (see more in Ref. [2]) into account. Since the response time to the operation (1b+) is finite, characterized in general by the sound speed c, it is hard to estimate the errors. Numerical experiments were performed with such 'zeroth order' algorithm against the 'semi-analytical' one, showing that the former leads to inaccurate results with growing errors from the inconsistent response between the density/pressure and the imposed Eq. (1b+): Fig. 4 constrasts the typical structures of $\partial_x(\ln\rho)$ and $\partial^2_{xz}(\ln\rho)$ resulting from the two algorithms at some early stage of the simulations, showing that the 'zeroth order' algorithm is poorly in accord with the precise result, $\partial^2_{hz}(\ln\rho) = 0$, of RSF and that 'semi-analytical' is precise (up to the pure 'noise' of numerical errors from discretization and

computer round off): the structures of $\partial_x(\ln\rho)$ from the former present obviously visiably deviatiations from perfect vertical 'bars' as those from the latter, and the difference of the errors in this respect is of 15 orders of magnitude, as indicated by the legends. Comparisons of $\partial_y(\ln\rho)$ and $\partial^2_{yz}(\ln\rho)$ is of similar character and not shown.

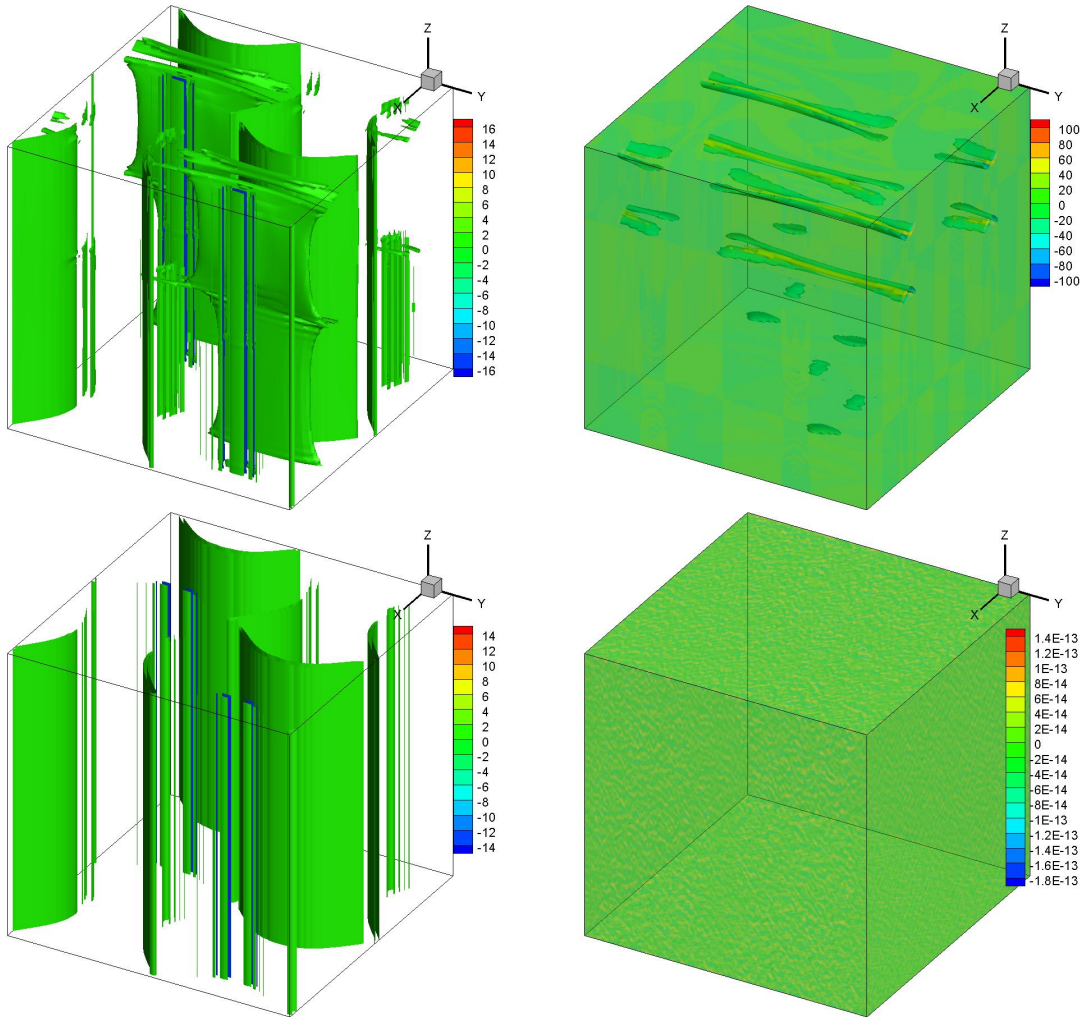

FIG. 4: Snapshots of the isosurfaces and contours (transluency) of $\partial_x(\ln\rho)$ (left) and $\partial^2_{xz}(\ln\rho)$ (right) for the 'zeroth order' algorithm (upper) and the 'semi-analytical' algorithm (lower) from test simulations of inviscid RSF starting from Eq. (20).

IV. RESULTS

In this section we present the solutions to the physical problems formulated in Sec. III A. The focuses are on the differences between production of small eddies from helical and

nonhelical TGF-fashion initial fields, and on the differences between the viscosity models, (6 and 5). A comparion between RSF and the Navier-Stokes flow (NSF) is also made.

All simulations were performed with initial $Re = 350$ and $Ma = 1$.

A. Multi-scale excitations of RSF eddies from 2C2Dcw1C3D initial fields

First of all, since the flow is completely new in the sense of realizations (*in silico*), we present in Fig. 5 for general conception the comparison of the fields at the very early time $t = 0.3$ between RSF and NSF starting from the same field of Eq. (20) and Fig. 1 at $t = 0$, showing very different evolution routes. Obviously, NSF immediately generates 3D $\boldsymbol{u}_h$, together with other differences to RSF.

To see the differences when the systems maturize with 'fully developed' multi-scale excitations, we also present in Fig. 6 the NSF fields and spectra at $t = 5$ (left and middle panels) for comparison:

$$E(k) := \sum_{|\boldsymbol{k}|=k} |\hat{\boldsymbol{u}}(\boldsymbol{k})|^2, \;\; {}^{v}E_v(k_v) := \sum_{|k_3|=k_v}^{\boldsymbol{k}_h} |\hat{\boldsymbol{u}}_3(\boldsymbol{k})|^2 \text{ and } \;\; {}^{h}E_h(k_h) := \sum_{|\boldsymbol{k}_h|=k_h}^{k_3} |\hat{\boldsymbol{u}}_h(\boldsymbol{k})|^2 \qquad (27)$$

where $\boldsymbol{k}_h := \{k_1, k_2\}$ which can be 'trivially' extended to be a 3-space vector $\{k_1, k_2, 0\}$. Actually, we notice that at such a moment the system has not really reached the 'mature' state, with an approximate $k^{-5/3}$ (which is generally referred to the Kolmogorov 1941 – K41 – law [31]) scaling in the potentially inertial range, which happens at $t = 6$ as shown by the right panel: It appears that all NSF spectra maturize (approximately) to the $k^{-5/3}$ law in the potentially inertial range where large-scale forcing (if exists) and small-scale damping effects are neglegible. Although multi-scale excitations present and the spectra appear like those of the conventional turbulence, we note that obvious order represented by the 'precise' (up to numerical errors) symmetry of the pattern inhereted and developed from the original field is in the flow. Such a characteristic, shared by all the results presented in this note, is not that of 'statistical symmetry' in the conventional (multi-)fractal or fully developed turbulence theory [31]. This observation also means that it makes sense to compare the definite flow structures of our simulations at the same moment. We will nevertheless keep making remarks related to 'turbulence' during the discussions of our results, and we believe they indeed are relevant.

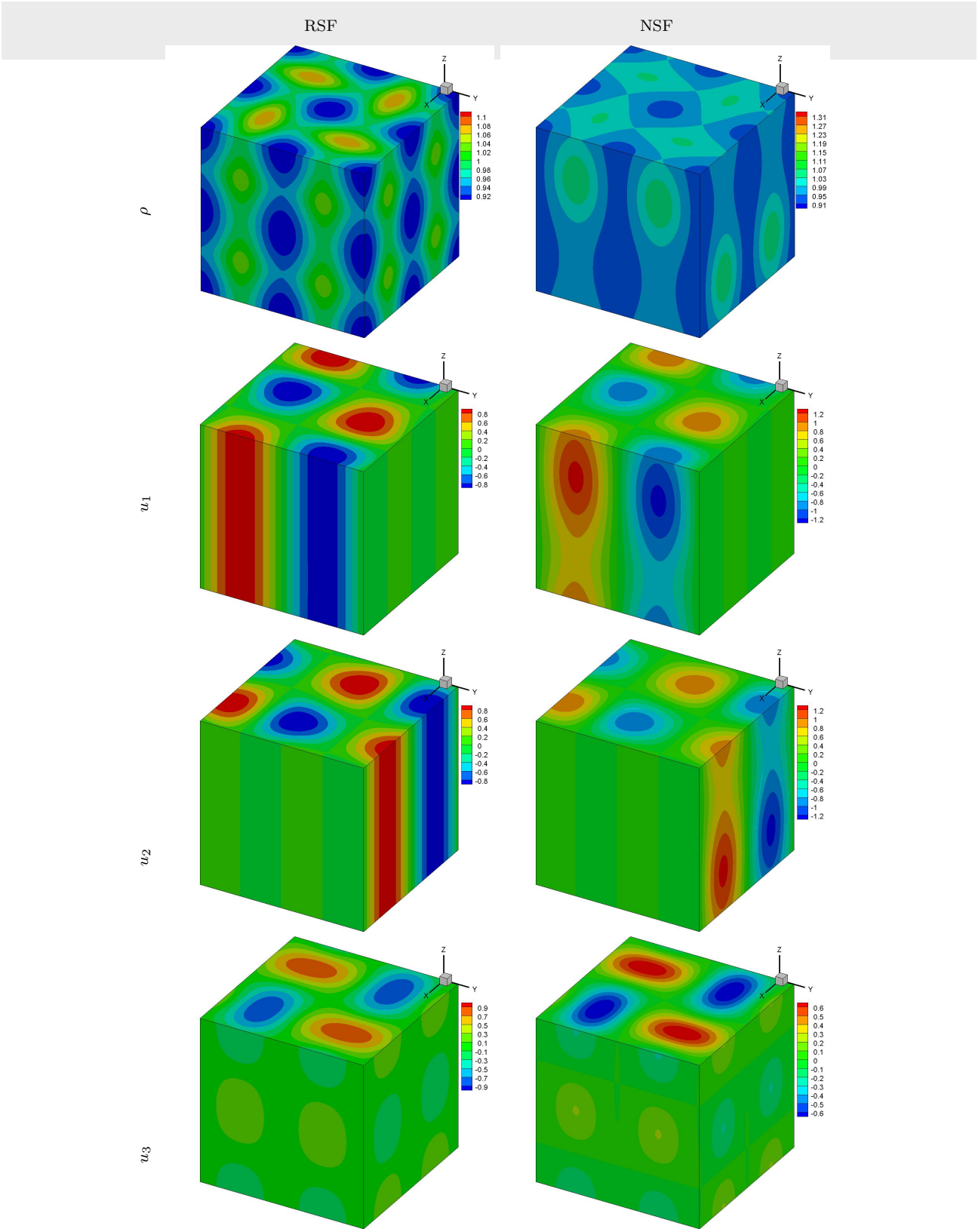

FIG. 5: Contours of the primitive variables ρ, u_1, u_2 and u_3 at $t = 0.3$, for NSF and RSF.

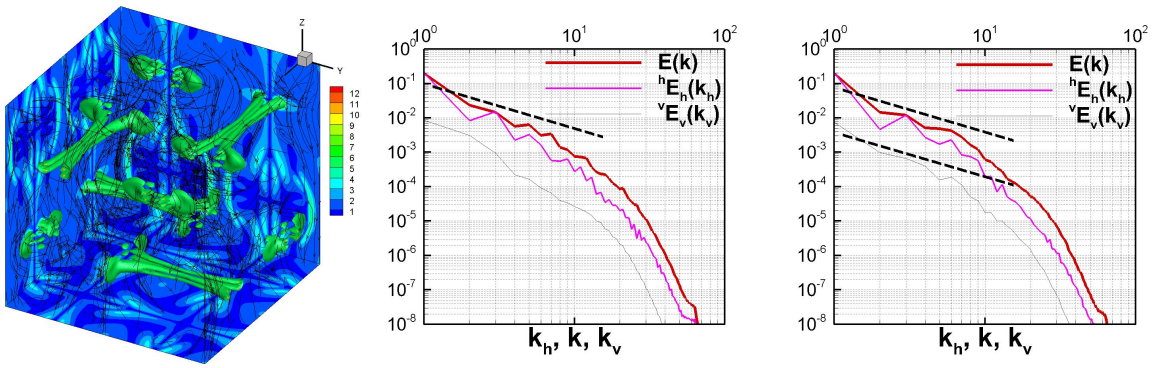

FIG. 6: Isosurfaces, slices of vorticity amplitude and streamtraces of vorticity (left), and, the power spectra of velocity (middle) of NSF at $t = 5$. Also presented are the corresponding spectra at $t = 6$ (modes of noninteger k are always grouped to the nearest integer shell, thus those of $k = \sqrt{2}$ are counted on the first shell, if not particularly pointed out as in a figure below). Dashed lines denoting $k^{-5/3}$ law are for reference.

Very differently, as shown in Fig. 7 (the power spectra and fields correspond in the two upper rows for three different simulations for the same flow, respectively, to those of Fig. 6), RSF runs into a completely different state, both in terms of patterns and velocity power spectra. The three columns are respectively from three different simulations with band-optimized symmetric WENO (WENO-SYMBO [21]: left) and WENO-Z ([20]: middle) for the RSF with Stokesian viscosity without the compressibility effect, and, with WENO-SYMBO for the RSF with full Stokesian viscosity. These results indicate on the one hand that the differences from the details of the different numerical schemes are small and irrelevant to our discussions, and, on the other hand, our semi-analytical algorithm, though precise (up to the numerical errors) only for the simplified viscosity, is actually very close and physically relevant to the 'real' Stokesian one. In other words, our algorithm is 'precise' also for the Stokesian viscosity, up to the errors of the applied numerical schemes which have already paid particularly attentions to the numerical dissipation problem with reasonable success.

Also presented in the lowest row of Fig. 7 are the density isosurfaces and slices, for which, just as in the figures for spectra, regions are circled out to highlight the tiny differences in the patterns. Such differences from numerical schemes or physical viscosity models are negligible for both verification of our algorithm and discussions of our results, such as the

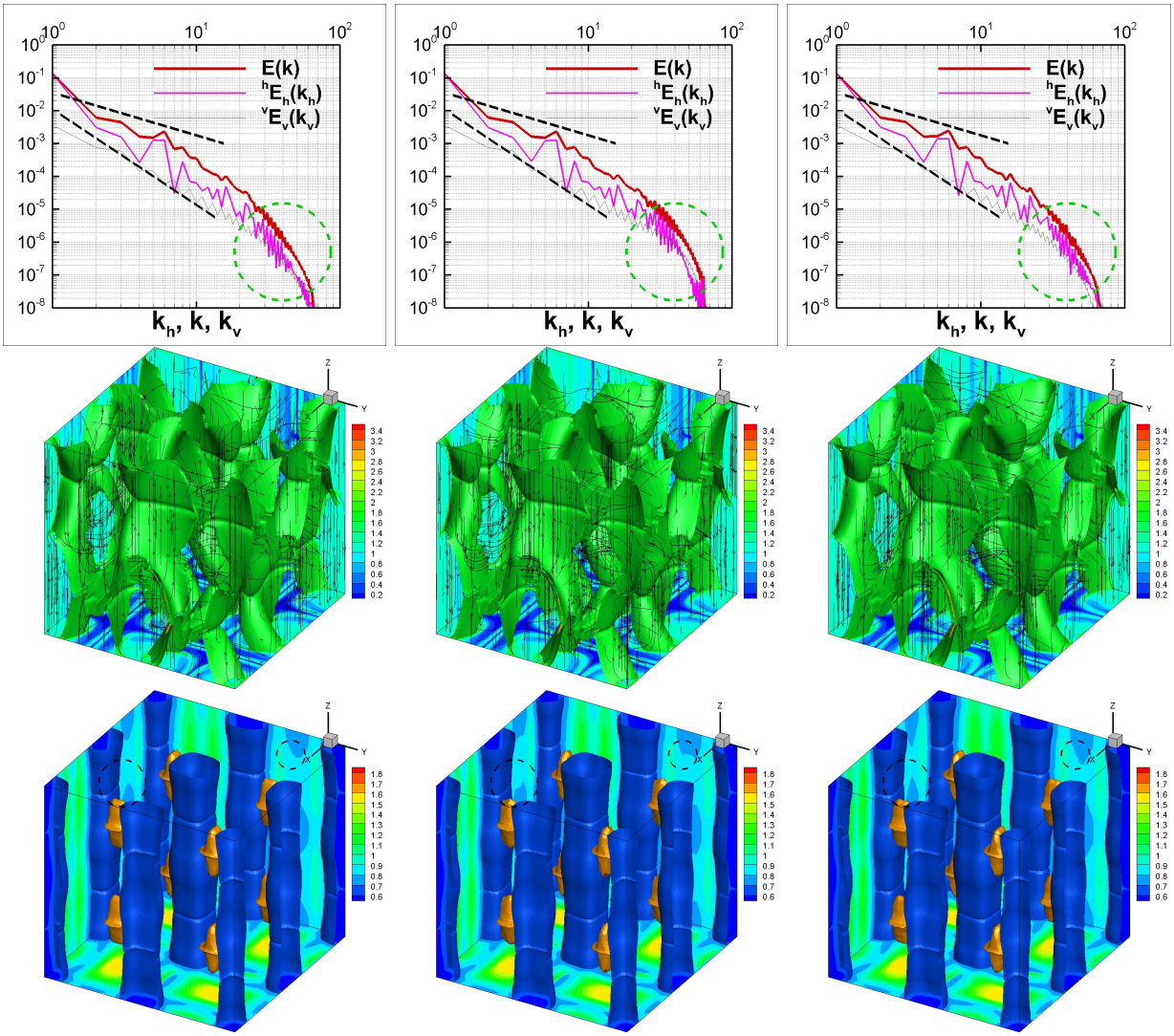

FIG. 7: Slices and isosurfaces (of values 0.7 and 1.7) of density at $t = 5$, showing tiny differences from different numerical schemes. Actually, the WENO-SYMBO (left) produces maximum 0.532881 and minimum 1.82369, while WENO-Z (middle) 0.532842 and 1.81667, a difference smaller than 0.4%. On the right panel, we also present the corresponding result from the Stokesian model simulated with the same strategy and algorithm described in Sec II C and the WENO-SYMBO finite difference scheme, and, again, only very small difference can be seen, with the maximum 0.53096 and minimum 1.82017, roughly of errors $2\% \sim 4\%$. Dashed lines denoting for $k^{-5/3}$ and k^{-3} laws in the top panels are also plotted for references, and some cirles are used to highlighted the regions where one can see the small differences.

general features of RSFs and the specific effects of helicity.

Before going into the even more specific discussions on the helicity effects on RSF multi-scale excitations of RSF eddies, we remark that although the RSF $E(k)$ appears to also maturize into a (approximately) $k^{-5/3}$ scaling law (designated with a slashed line) in the potentially inertial range, the vertical spectrum of vertical velocity ${}^{v}E_{v}(k_{v})$ does not. The latter appearing to be k^{-3} (also designated with a slashed line), as will be further addressed.

B. Multi-scale excitations of RSF eddies from 3C2D initial fields

We now turn to compare results from the simulations started from the nonhelical and purely helical (actually Beltrami with monowavelength) RSFs described by Eqs. (21, both assisted by 23) with $\epsilon = 0.35$. The viscosity model satisfies Eq. (6).

1. The general spectral dynamics

Before everything, we should point out that, since our initial RSF has wavenumber $k = \sqrt{2}$, counting it on the first or second integer shell, and similarly other modes for other shells, for plotting the spectrum presents different results. Thus, when interpreting our results, especially for small k, we should always be careful about this, which is the reason we have plotted the results with two different ways, one in Fig. 8 with such modes on the second shell (and similarly for others for which the issue is less critical with larger k) and the other (for all the other plots in the work) with these modes counted on the first shell.

Since the field can be decomposed into left-, right- and nill-handed modes corresponding to the eigenvalues $-k$, $+k$ and 0 of the curl operator, $\hat{i}\boldsymbol{k}\times$ in the Fourier space (see also the representation with Craya-Herring-Cambon coordinate [33]), it is natural to look first at the spectral behaviors of such sectors in Fig. 8, for which we define left- and righ-handed spectra

$$EL := \sum_{|\boldsymbol{k}|=k} |{}^{L}\hat{\boldsymbol{u}}(\boldsymbol{k})|^2 \text{ and } ER := \sum_{|\boldsymbol{k}|=k} |{}^{R}\hat{\boldsymbol{u}}(\boldsymbol{k})|^2 \tag{28}$$

from which we can compute the spectra of the nill-handed (parallel/potential) mode and helicity

$$P(k) = E - EL - ER \text{ and } H(k) = k(ER - EL). \tag{29}$$

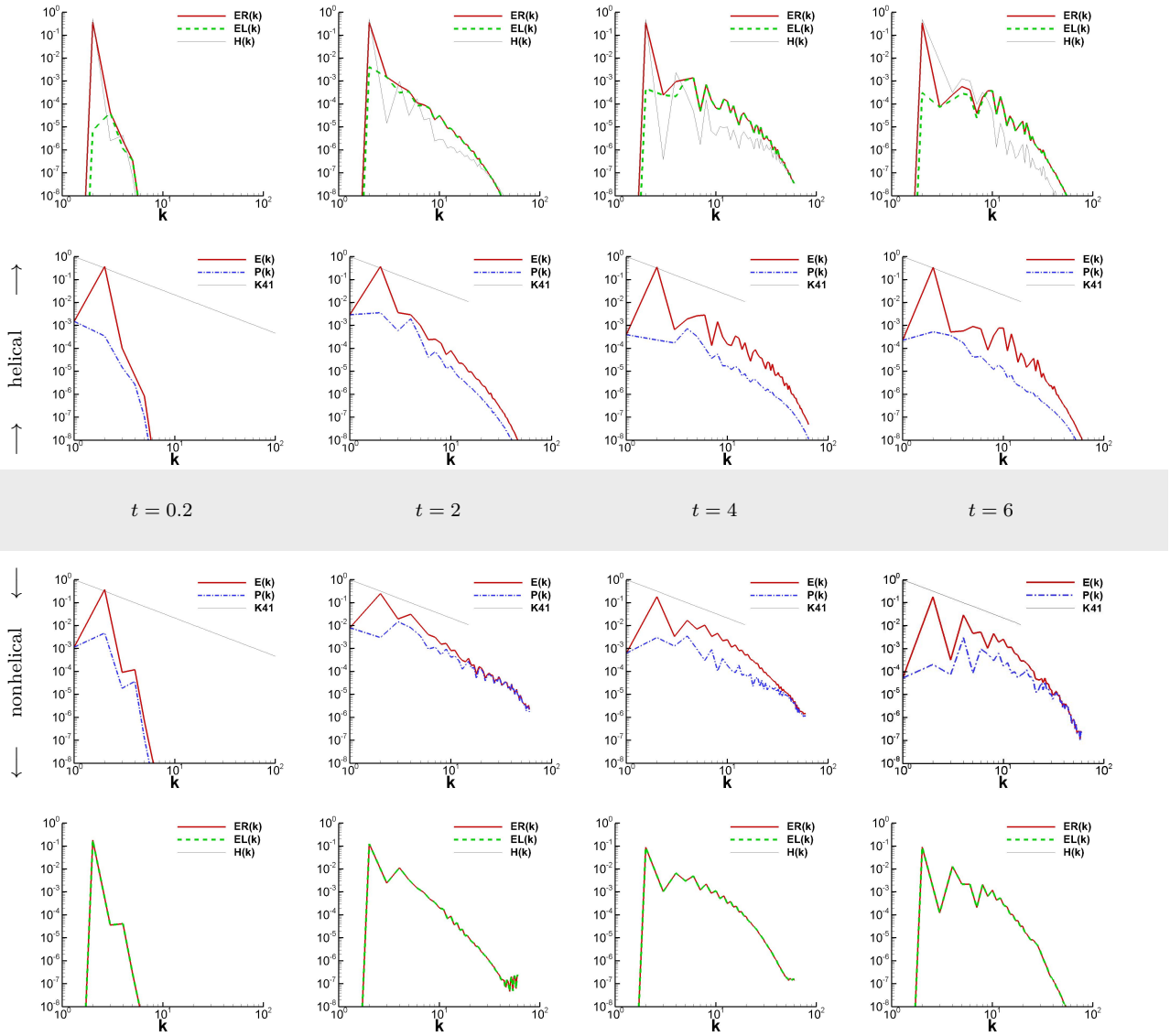

FIG. 8: The velocity, its left-, right-handed and parallel eigenmode power spectra $E(k)$, $EL(k)$, $ER(k)$ and $P(k)$ at different times for the helical and nonhelical cases, together with the Kolmogorov scaling law ("K41") for reference in some plots.

The two rows above the shaded box containing time labels for each column are for the results from helical RSF, and those below for the nonhelical case. The total spectrum $E(k)$ and the K41 $k^{-5/3}$ law are also plotted for reference. Note that in the last row the helicity spectra are zero (up to the numerical errors) and not visible in the windows of the layouts.

We observe *i)* the early excitation of modes by the initial ones ($t = 0.2$), *ii)* most available modes being well excited but still far from the "equilibrium" ($t = 2$: the velocity spectrum is approaching but obviously not close to the K41 law), *iii)* premature "equilibrium" state

with inertial and dissipation ranges almost but not yet established very well ($t = 4$) and *iv)* the mature equilibrium state with all excitation established as possible and the dissipation having been systematically reducing the whole level of spectrum ($t = 6$). After $t = 6$, the system is going towards the so-called 'late-time' decaying regime which is not of our interest here. As mentioned, the initial-field modes are of wavenumber $k = \sqrt{2}$, but for the presentation of spectra, they are counted in the $k = 2$ shell here. We should focus on the activities of the modes beyond this 'thermal bath' shell (remember that the z-coordinate dependence are originally driven by the density/pressure gradient along this direction). Note also that we have adopted the scenario and terminology for turbulence and based our choices and remarks on the emperical observations and judgement, although the system still presents highly precise order, especially the symmetries in the patterns (see below). There has not been a rigorous theory [31] for the inertial scaling law such as the K41 one, not even a consensus on the complete definition of turbulence, but we just chose a 'pragmatism' standpoint for the purpose of describing the multi-scale eddies in the above.

It is seen in Fig. 8 that the right-handed initial RSF evolves into that with all three sectors, but ER keeps dominating the energetic behavior, especially before entering the dissipation scales (where the amplitudes of left- and right-handed modes are relatively closer), with $H(k)$ being positive definite; while, the nill-handed initial RSF keep nill-handed, never loosing the symmetry as time goes.

Interestingly, the parallel modes of the helical case are less excited, both in the absolute and relative senses, the ratio $P(k)/E(k)$ for the relative value being simply measured by the vertical distance between the two spectral lines in the logarithmic coordinates for the plots [easily observable with bare eyes by comparing the areas between the lines of $P(k)$ and $E(k)$], except for the first two shells at $t = 6$, which is consistent with the mechanical/geometrical and statistical analyses, and, the 'fastening' notion proposed earlier [6]: the gravest modes of $k = 2$ counted on the second shell serve as the 'source', of energy and helicity, for the other modes, thus the time variations of the modes on it and the nearest shells may need additional theoretical considerations.

Since RSF is apparently anisotropic, the above general 1D spectral analysis is of course not complete, as already indicated in Sec. IV A, and more specific spectral results will be analyzed in Sec. IV B 3 before which we would like to present the general patterns of such RSF evolutions.

2. The general flow patterns

Fig. 9 presents the evolutions of density contours for the helical and nonhelical RSFs, showing consistently, with the previous spectral observation, especially the compressibility-relevant parallel-mode spectra, that, over all, the density-modes are less excited. Especially, the nonhelical case can have the maximum and minimum values far beyond the initial ones, indicating the production of strong expansion regions and compression (probably shocks), which will be further examined:

We now focus on the moment at $t = 6$, when the snapshots of the isosurfaces and slices of ρ and $|\nabla\rho|$ are captured in Fig 10: the high(est) density regions are in general accompanied with the stong(est) gradients at almost, but not exactly, the same places, thus demonstrating the shocks with the isothermal density being essentially the pressure. The nonhelical case presents much stronger shocks with much more sharply 2D structures. In Fig. 11, we zoom in close to the strong gradient regions, rotate the axis for better observation, and plot the rakes of velocity streamtraces, showing that the nonhelical case indeed presents (almost) 2D surface of shock with abrupt deflection of the streamlines across it and that the helical case prsents a much thicker spatial domain accrossing which the streamlines, also oblique, do not present any obvious deflection (thus not close to a real shock). The shocks are clearly seen to be much less space occupying, an indication of (strong) spatial intermittency, and most of the space are occupied by expansion regions with density close to the background value and low weak gradients. The stronger/more intermittent the shocks are, the more space weak $|\nabla\rho|$ occupies. Note that, though rationally natural, the conjecture and remarks relevant to shocks in Ref. [6] went much beyond the arguments supporting the analysis made there: the analytical tractability of the statistical mechanical calculation required weak excitation assumption and that of geometrical analysis took the inviscid limit. Thus, the results about shocks presented here is not only an obvious support but also a strong indication of a more systematic theory behind it.

We have explained in Sec. III A that the helical initial field is Beltrami, thus its $\boldsymbol{u}$- and $\boldsymbol{\omega}$-streamtrace patterns are exactly the same as presented there. Here, although, the helical case is not Beltrami, actually not even purely helical (homochiral), any more as time goes, the vorticity- and velocity-streamtrace patterns in the helical case, unlike the nonhelical one, look still quite similar in Fig. 10, at least at large scales, except for some small-scale details,

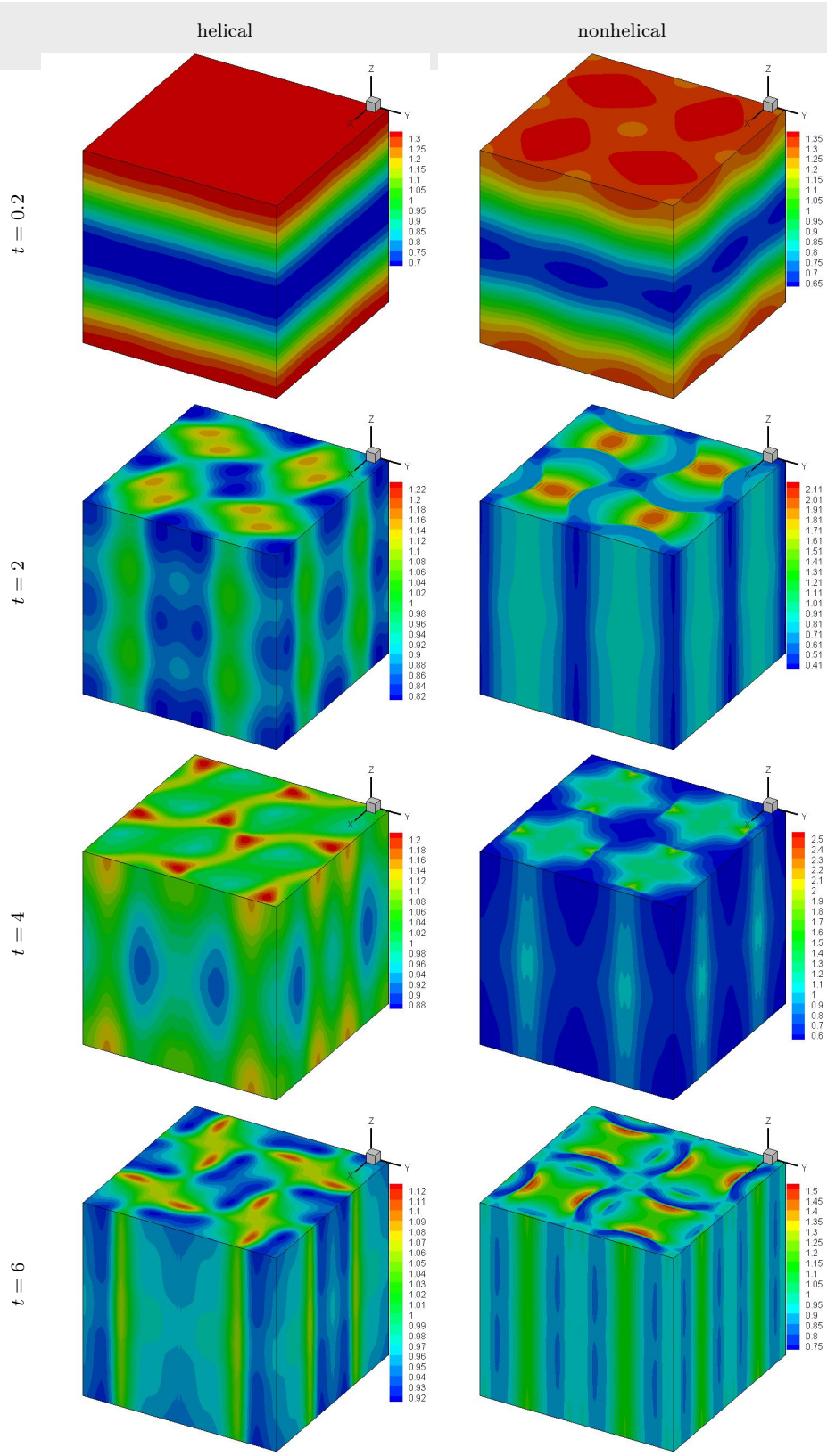

FIG. 9: The density contours.

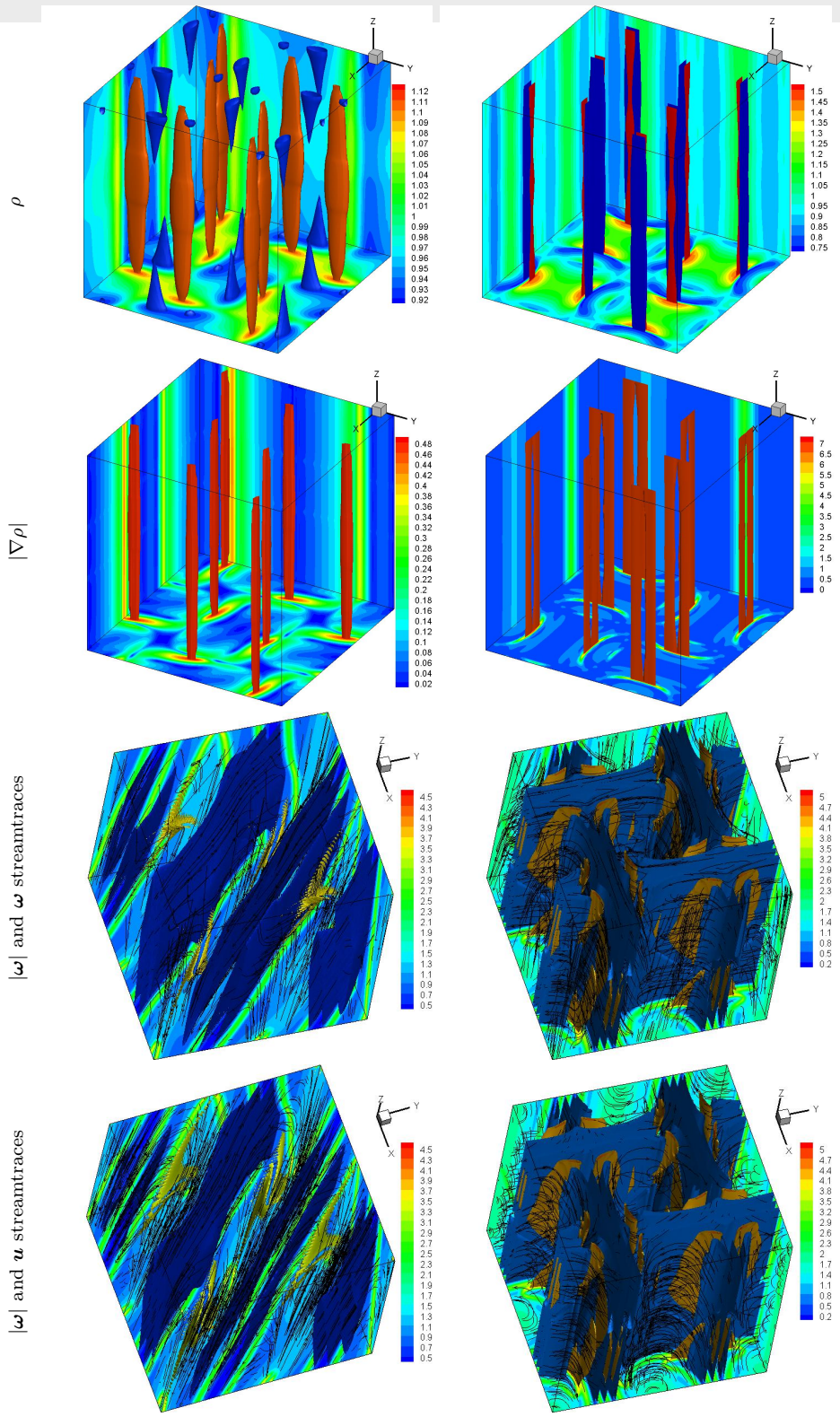

FIG. 10: Patterns at $t = 6$.

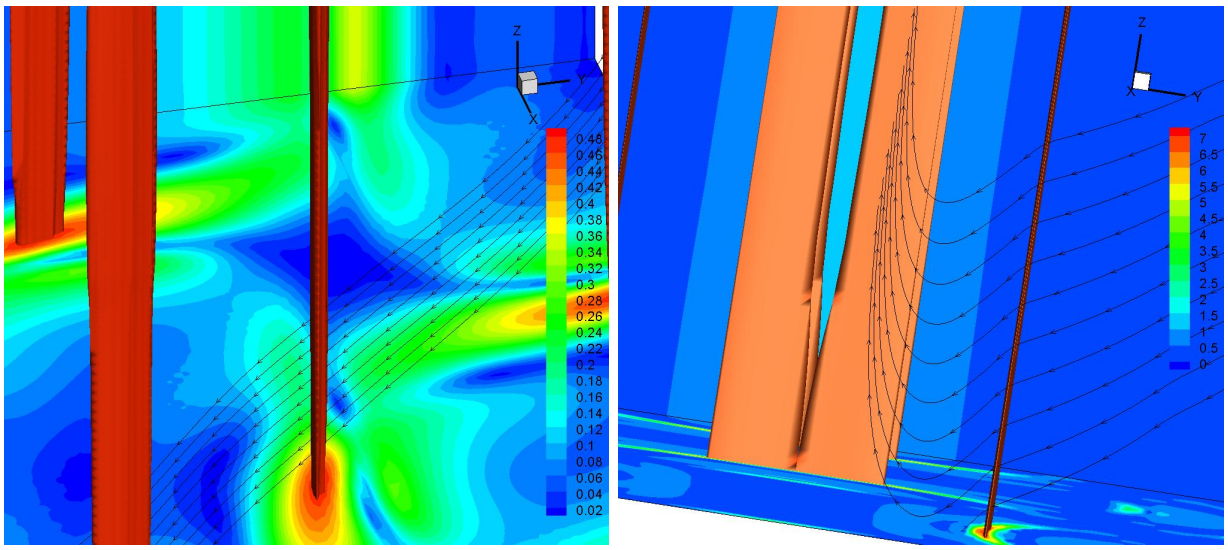

FIG. 11: Velocity Streamtraces across the strong density gradient regions for the helical (left) and nonhelical (right) cases.

which should not be surprising, because, as shown in Fig 8, at each moment, most of the helicity is concentrated on the $k = 2$ shell where the right-handed and left-hand energies are of a difference of (more than) three orders of magnitude, thus basically homochiral and Beltrami. The corresponding nonhelical patterns, in contrast, do not have such properties.

Note that, although RSF allows the x_3 dependence of u_3, which, however, in the classical setting is of the 'parallel mode' nature and in most spatial regions, as indicated by the above density discussion, should be small. Thus, RSF in general appear over all much of 2D characteristic. One can start with an RSF of very large $u_{3,3}$, in which case u_3, compared to $\boldsymbol{u}_h$, will also be subjected to an additional damping operator $\nu\partial_{33}^2$ according to the viscosity model (6) and eventually will be weaker.

3. More specific analyses

As remarked, RSF is by definition anisotropic, and the patterns of some quantities such as the $\boldsymbol{u}$ streamlines and those related to the density presented in Sec. IV B 2 appear to be quite of 2D character though in principle can be 3D. Thus, the general spectral dynamics presented in Sec. IV B 1 are not specific enough to describe RSFs, and according to RSF nature and our initial data we will look more into the details of the anisotropic properties.

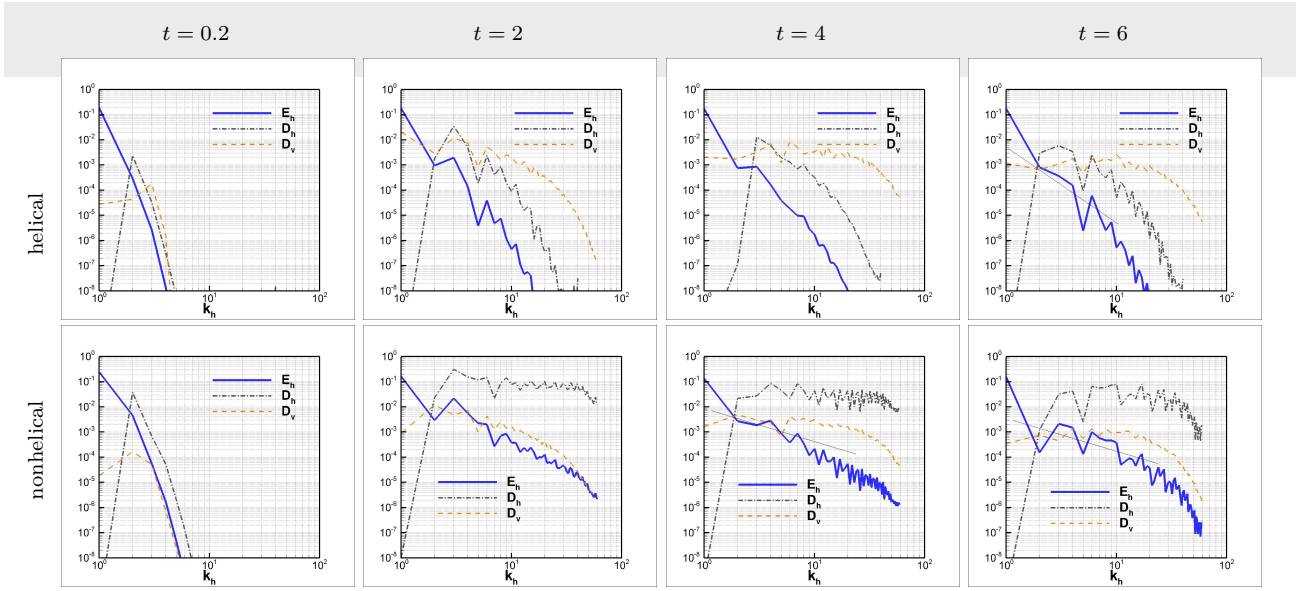

FIG. 12: The horizontal energy and divergence spectra, and, the vertical divergence spectra. Kolmogorov scaling law denoted by straight lines are also added to some plots for reference.

First of all, since the RSF $\boldsymbol{u}_h$ is 2D, depending only on the horizontal wave vector $\boldsymbol{k}_h$, we should examine the relevant spectra in terms of k_h. Fig. 12 presents the 'horizontal spectra', corresponding to the results discussed in Secs. IV B 2 and IV B 1,

$$E_h(k_h) := \sum_{|\boldsymbol{k}_h|=k_h} |\hat{\boldsymbol{u}}_h(\boldsymbol{k}_h)|^2 \text{ and } D_h(k_h) := \sum_{|\boldsymbol{k}_h|=k_h} |\hat{\boldsymbol{u}}_h(\boldsymbol{k}_h)\cdot\boldsymbol{k}_h|^2, \tag{30}$$

which measure the 'power' of the fluctuations of, respectively, $\boldsymbol{u}_h$ and $\nabla_h\cdot\boldsymbol{u}_h$ on each horizontal wave number k_h. [Note that the modes with $k_3\neq 0$ for $\boldsymbol{u}_h$ are truncated by the definition of RSF.] Compared to the comparisons for the helical and nonhelical cases in Fig. 8, it is seen that here the $\boldsymbol{u}_h$ small eddies are even more markedly less excited: while $E(k)$ there nearly reaches a $\propto k^{-5/3}$ state at $t=6$ in the 'potentially inertial' range (roughly for $2<k<10$), here $E_h(k_h)$ is much steeper, as can be seen by the thin solid black line denoting $\propto k^{-3}$ and added for reference. $D_h(k_h)$ also shows that horizontal small eddies are much less compressible. These horizontal behaviors are in sharp contrast with the nonhelical case where thin black lines denoting $\propto k^{-5/3}$ are added to the plots at $t=4$ and $t=6$. The vertical divergence spectrum

$$D_v(k_h) := \sum_{|\boldsymbol{k}_h|=k_h,k_3} k_3^2|\hat{u}_3(\boldsymbol{k}_h,k_3)|^2 \tag{31}$$

also appears to be slightly affected by the helicity, but much less than $E_h(k_h)$ and $D_h(k_h)$. Although such reduction of horizontal compressibility appears to be consistent with an argument given in Ref. [6], of boosting to a rotating frame in which the helicity vanishes and thus transforming the helicity effect to the rotation effect (Taylor-Proudman effect of reducing compressibility in the rotating plane), the additional detailed observations, such as the $E_h(k_h)$ spectral behavior, deserve further theoretical consideration according to the dynamics. [A consistent consideration of 'compressibility' involves normalization, say, by the enstrophy or total spectrum: c.f., the remark for Fig. 8 on the relative reduction of $P(k)$.] Here, we offer a possible theoretical scenario in the context of turbulence as follows.

The $\boldsymbol{u}_h$ dynamics in the isothermal RSF model used in our simulations is controlled by Eq. (1b-) which is almost autonomous except that the pressure gradient is coupled to the rest of the system through the density. Now, if the pressure gradient is assumed to be decomposed into two parts, one corresponding to that in the incompressible 2D flow (thus solving the Poisson equation with the source being the divergence of the nonlinear term) and the other being externally affected and serving as the pump for $\boldsymbol{u}_h$. If the pumping is concentrating at some large scales and the $\boldsymbol{u}_h$ is approximately incompressible, a forward enstrophy transfer together with an E_h spectrum $\propto k_h^{-3}$ (with logarithmic correction) is then the well-tested incompressible 2D turbulence theoretical result [34]. In other words, the rest of the system may offer an environment of external nonlocal-transfer channels while still facilitating a genuine internal local direct transfers of the 2D incompressible flow nature. How Eq. (1b-) couples with the rest of the system can be very subtle due to the multi-scale and nonlocal nature of pressure/density fluctuations, and the characteristics at $t = 6$ in Fig. 12 for the helical case is of course not yet clear and clean enough; and, much more systematic investigations with general initial fields, including an ensemble of random ones, other than the specific one we treated here are needed to test such a speculation.

We then present in Fig. 13 the spectra of $u_v := u_3$, as functions of k, k_h and k_v,

$$E_v(k) := \sum_{k=|\boldsymbol{k}|} \frac{|\hat{u}_v|^2}{2}, \quad {}^hE_v(k_h) := \sum_{k_3,k_h=|\boldsymbol{k}_h|} \frac{|\hat{u}_v|^2}{2} \text{ and } {}^vE_v(k_v) := \sum_{\boldsymbol{k}_h,k_v=k_3} \frac{|\hat{u}_v|^2}{2}, \quad (32)$$

which characterize the distributions and variations of, respectively, the vertical velocity, u_v, eddies in full 3D space, in the horizontal plane and along the vertical coordinate. We now see that the u_3 dynamics are not so much different for the helical and nonhelical cases as for $\boldsymbol{u}_h$. Especially, the ${}^vE_v(k_v)$ behaviors are very close, both presenting a quite clean $\propto k^{-3}$ law at

large scales (thin lines of such a scaling are added to the plot for reference), and only at $t = 6$ the helical ${}^{v}E_v(k_v)$ is at a slightly higher level (while those of $E_v(k)$ and ${}^{h}E_v(k_h)$, both being close, are lower, beyond the first shell). Reference lines of $\propto k^{-5/3}$ are also added to the plots, denoting the possible (approximate) behaviors of $E_v(k)$ and ${}^{h}E_v(k_h)$ in the potential inertial range: just as before, doing this, we by no means indicate the precise results in the asymptotic inertial range, with or without corrections from intermittency or other physical reasons. No strong theoretical suggestion, relevant to passive scalar or acoustics, is offered for the k^{-3} scaling either. We believe these results, though coming only from the very specific initial fields, are fundamental and important, with no available directly relevant theory for explanation, to our best knowledge, and should be simply presented for information and motivation.

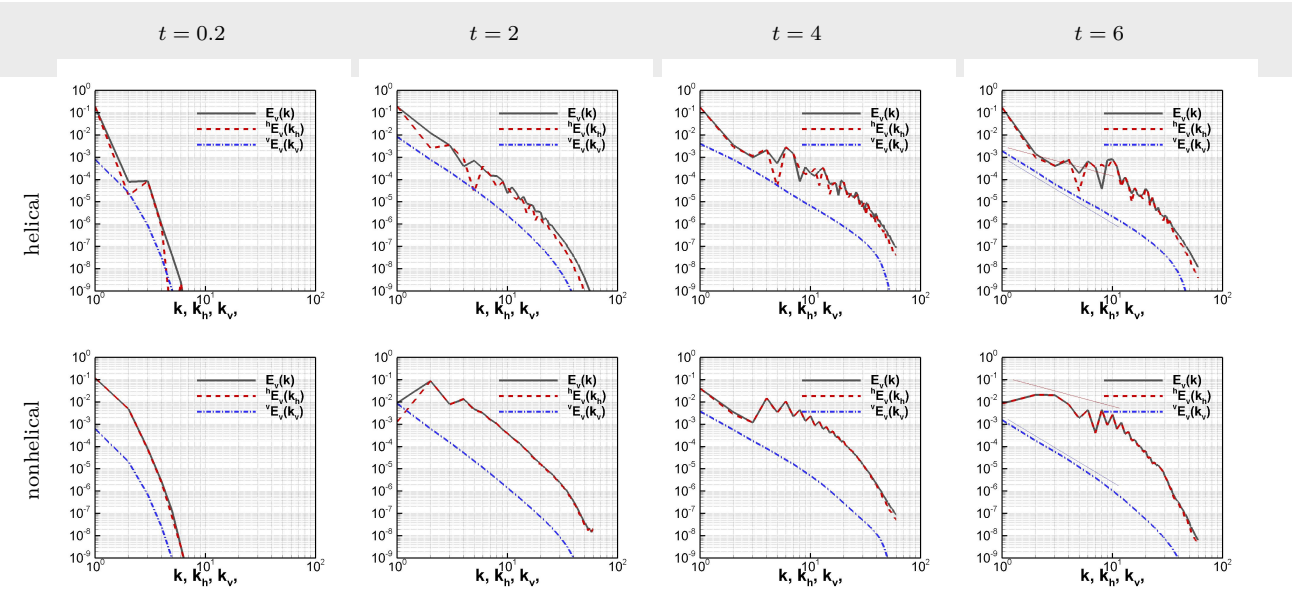

FIG. 13: The velocity spectra E_v, ${}^{h}E_v(k_h)$ and ${}^{v}E_v(k_v)$. Thin straight lines for laws $\propto k^{-5/3}$ and $\propto k^{-3}$ are added to some of the plots for reference.

V. FURTHER DISCUSSIONS

RSF being new and anisotropic, many more results can be still of some value to be demonstrated. For example, we may analyze the vertical and horizontal helicity, dissipation and density spectra, and, also the anisotropic higher-order structure functions of various variables. We may also analyze the longer (late) time evolution, such as the anisotropic

decaying rates, the homogeneization processes, and so on and so forth. However, to make all that more meaningful, we also need more mathematics and theory, as some of the results presented here already call for. Thus, it is important to leave some space for thought experiments and excursions here, before which let us summarize what have been reaped and what should be the stratigic direction:

We have formulated the numerical RSF problem and showed that the precise analytical results of RSF established in Ref. [2] can be used to design effective semi-analytical algorithm for simulation. Explicit physical problems of the TGF and ABCF fashions have been created for proof-of-concept examples. The numerical results demonstrated the evolution of RSF distinct from that of NSF, the excitation of multi-scale RSF small eddies. Recent theoretical arguments and conjectures about the helicity effect on reducing the compressibility of the flow have been tested, and actually extended in a firm way. The differences from different numerical discretization schemes are shown to be so small that they are irrelevant to the general conclusions about the production of small eddies and the helicity effects.

It is promising to further apply the algorithm to carry out the studies of RSF turbulence, forced or decaying, with other possibly more precise methods (such as the pseudo-spectra one) and higher resolutions, and/or, longer-time simulations developing further from the results presented here or starting from random fields. Such studies could shedlight on the passive scalar and rotating flow issues, for the obvious connections of RSF with the Taylor-Proudman limit.

Further more, the formal compressible Taylor-Proudman theorem [6] requires the incompressibility of $\boldsymbol{u}_h$, thus it is also interesting to extend the algorithm to such flows and to carry out the numerical studies of such even more special RSFs, turbulent or not.

On the other hand, although it appears in the case presented in Sec. IV B that the RSF with Stokesian viscosity taking the velocity dilatation into account, simulated with our semi-analytical algorithm, is also very close to that without the compressibility effect in the viscosity model, such a situation is not assured for every other case, especially for turbulence at very high Reynolds numbers and/or very large Mach numbers, and, for other flows (such as the non-newtonian fluid and quantum flows [35]) beyond the Navier-Stokes framework. Thus, other effective brute-force algorithms more universally applicable for general RSF simulations are also desired.

Indeed, for the nonbarotropic RSF, a set of precise relations for the temperature structures

can also be established [2] and be used to check the errors by measuring the deviations from them, just as we showed in Fig. 4 for the density structure. Preliminary numerical experiments show that our algorithm can also simulate such RSFs reasonably well: this is not like the situation for the 'zeroth order' algorithm discussed with that figure, because our semi-analytical algorithm already ensures the part of the thermodynamic structure and the difference of the temperature from our algorithm to the precise one in general moderate cases do not affect the flow too much (part of the reason why the isothermal process can be a good approximation). Of course, in principle, especially for turbulence at high Re and Ma where entropy modes are crutial and the fine structures are important for particular interests or problems, we should have a self-consistent algorithm with such equations like (1a and 1b) that the relevant errors are completely under control, which deserves further studies.

To see how interesting and challenging, to our understanding, the open problem we set out is, let us elaborate a bit by taking some results from Ref. [2]: For an ideal gas with, say, $p = \rho\mathcal{R}T$, Eq. (10) reads

$$\Big[\frac{\nabla_h(\rho T)}{\rho}\Big]_{,3} = 0. \tag{33}$$

Eq. (33) indicates that $\frac{\nabla_h(\rho T)}{\rho}$ is a function of only x_1 and x_2 and should have such separation of the variables

$$\rho = r(x_3)/R(x_1, x_2) \tag{34}$$

that the numerator r and denominator R can cancel the common factor $r(x_3)$. In other words, we have the same structure, especially Eq. (1a), as in the isothermal case. And, by taking (34) into (33), we further have

$$T(x_1, x_2, x_3) = \mathcal{T}(x_1, x_2) + R(x_1, x_2)\tau(x_3), \tag{35}$$

where $\mathcal{T}$ and τ and other variables are also time dependent. Eq. (35) characterizes the very fine structures of T, and designing an effective algorithm for it, semi-analytical or brute-force, appears to be a nontrivial challenge. More definite derivatives from Eq. (35) have also been offered in Ref. [2], but, here, it is more appropriate to leave the space for imaginations.

ACKNOWLEDGMENTS

Messrs H. Ren and C. Tang subsequently participated in some numerical experiments with other algorithms we tried in the early stage of the work, such as the 'zeroth order' scheme addressed in Sec III B, back in 2018 [36] immediately after the flow was discovered [37]. We also thank Y. Zhang for sharing the well-structured code with different schemes for shock capturing, useful for the "standard-CFD part" of the RSF solver.

BIBLIOGRAPHY

[1] G. I. Taylor, A. E. Green, Mechanism of the production of small eddies from large ones, Proceedings of the Royal Society of London. Series A, Mathematical and Physical Sciences 158 (1937) 499–521.

[2] J.-Z. Zhu, Thermodynamic and vortic fine structures of real Schur flows, submitted for publication; see also, arXiv:2103.10864.

[3] A. Jameson, Time Dependent Calculations Using Multigrid, with Applications to Unsteady Flows Past Airfoils and Wings, AIAA 91 (1991) 1596.

[4] M. A. Gallis, J. R. Torczynski, M. C. Krygier, N. P. Bitter, S. J. Plimpton. Turbulence at the edge of continuum, Phys. Rev. Fluids 6 (2021) 013401.

[5] Y. Bo, P. Wang, Z. Guo, L.-P. Wang, DUGKS simulations of three-dimensional Taylor–Green vortex flow and turbulent channel flow, Comput. Fluids 155 (2017) 9–12.

[6] J.-Z. Zhu, Compressible helical turbulence: fastened-structure geometry and statistics, Phys. Plasmas 28 (2021) 032302.

[7] M. E. Brachet, D. I. Meiron, S. A. Orszag, B. G. Nickel, R. H. Morf, U. Frisch, Small-scale structure of the Taylor–Green vortex, J. Fluid Mech. 130 (1983) 411–452.

[8] M. E. Brachet, D. I. Meiron, S. A. Orszag, B. G. Nickel, R. H. Morf, U. Frisch, The Taylor–Green vortex and fully developed turbulence, J. Stat. Phys. 34 (1984) 1049–1063.

[9] Z.J. Wang, K. Fidkowski, R. Abgrall, F. Bassi, D. Caraeni, A. Cary, H. Deconinck, R. Hartmann, K. Hillewaert, H.T. Huynh, N. Kroll, G. May, P.-O. Persson, B. van Leer, M. Visbal, High-Order CFD Methods: Current Status and Perspective, International Journal for Numerical Methods in Fluids, 72, (2013) 811–845.

[10] J.R. Bull, A. Jameson, Simulation of the Taylor–Green Vortex Using High-Order Flux Reconstruction Schemes, AIAA Journal, 53 (2015) 2750–2761.

[11] R. H. Kraichnan, On the statistical mechanics of an adiabatically compressible fluid, J. Acoust. Soc. Am., 27 (1955) 438.

[12] J. Shebalin, Pseudospectral simulation of compressible turbulence using logarithmic variables, 11th Computational Fluid Dynamics Conference (1993) Orlando, FL, U.S.A.

[13] Collaboration et al., The Pencil Code, a modular MPI code for partial differential equations and particles: multipurpose and multiuser-maintained, The Journal of Open Source Software, 6 (2021) 2807.

[14] J. J. D. Anderson, Computational Fluid Dynamics: The Basic with Application, McGraw-Hill, Inc. (1995).

[15] W. Sutherland, The viscosity of gases and molecular force, Lond. Edinb. Dubl. Phil. Mag. 36 (1893) 507–531.

[16] In the Stokesian viscosity model with the dissipation term $\boldsymbol{M}(\boldsymbol{u}) = \mu\nabla^2\boldsymbol{u} + \frac{\mu}{3}\nabla(\nabla\cdot\boldsymbol{u})$ for constant dynamical viscosity μ, we have instead $\partial_3(\frac{1}{\rho}\nabla_h\frac{\mu u_{3,3}}{3}) = \partial_3(\frac{1}{\rho}\nabla_h p)$, and more complex relations would be required for other non-Newtonian models.

[17] Y.-T. Zhang, C.-W. Shu, ENO and WENO Schemes, Handbook of Numerical Analysis (2016).

[18] G. S. Jiang, C. W. Shu, Efficient implementation of weighted ENO schemes, J. Comput. Phys. 126 (1996) 202–228.

[19] X.-L. Li, D.-X. Fu, Y.-W. Ma, Direct numerical simulation of hypersonic boundary layer transition over a blunt cone with a small angle of attack, Physics of Fluids, 22 (2010) 025105.

[20] R. Borgesa, M. Carmonaa, B. Costaa, W.-S. Don, An improved weighted essentially non-oscillatory schemefor hyperbolic conservation laws, Journal of Computational Physics 227 (2008) 3191–321.

[21] M.P. Martín, E.M. Taylor, M. Wu, V.G. Weirs, A bandwidth-optimized WENO scheme for the effectivedirect numerical simulation of compressible turbulence, Journal of Computational Physics 220 (2006) 270–289.

[22] S. Orszag and C. M. Tang, Small-scale structure of two-dimensional magnetohydrodynamic turbulence, J. Fluid Mech. 90 (1979) 129.

[23] U. Frisch, A. Pouquet, P. L. Sulem, and M. Meneguzzi, J. Mech. Theor. Appl., numéro spécial, 2D, 191 (1983).

[24] See, e.g., the test case of software Athena: https://www.astro.princeton.edu/~jstone/Athena/tests/orszag-tang/pagesource.html.

[25] H. Politano, A. Pouquet, and P. L. Sulem, Current and vorticity dynamics in three–dimensional magnetohydrodynamic turbulence, Phys. Plasmas 2 (1995) 2931.

[26] T. Dombre, U. Frisch, J. M. Greene, M. Hénon, A. Mehr and A. M. Soward, Chaotic streamlines in the ABC flows, Journal of Fluid Mechanics 167 (1986) 353–391.

[27] M. Lesieur, Turbulence in Fluids, 2nd ed. (Kluwer Academic, Dordrecht, The Netherlands, 1990).

[28] M. V. Melander, F. Hussain, Polarized vorticity dynamics on a vortex column, Physics of Fluids A 5 (1993) 1992.

[29] T. Passot, A. Pouquet, Hyperviscosity for compressible flows using spectral methods, Journal of Computational Physics 75 (1988) 300–313.

[30] S. Gottlieb, C.-W. Shu, Total variation diminishing Runge–Kutta schemes, Math. Comput. 67 (1998) 73–85.

[31] U. Frisch, Turbulence. Cambridge University Press (1995).

[32] J.-Z. Zhu, Isotropic polarization of compressible flows. J. Fluid Mech. 787 (2016) 440.

[33] C. Cambon, G. N. Coleman and N. N. Mansour, Rapid distortion analysis and direct simulation of compressible homogeneous turbulence at finite Mach number, J. Fluid Mech. 257 (1993) 641–665; P. Sagaut, C. Cambon, Compressible Homogeneous Anisotropic Turbulence, in Homogeneous Turbulence Dynamics (2018, Chapter 14) 691–725.

[34] G. Eyink, U. Frisch, Robert H. Kraichnan, in "A Voyage through Turbulence" P. Davidson, Y. Kaneda, H.K. Moffatt and K.R. Sreenivasan, eds. Cambridge Univesity Press (2011) 329–372; G. Boffetta and R. E. Ecke, Two-Dimensional Turbulence, Annu. Rev. Fluid Mech. 44 (2012) 427–451.

[35] For quantum flow equations such as the fluid equation from the well-known Gross-Pitaevskii equation through the Madelung transform or the quantum Navier-Stokes equation, the quantum pressure term and the viscosity in the latter case do not admit the precise relation established in Ref. [2] and additional wisdoms are needed to compute the corresponding RSF: we particularly point this out because of the quantum vortex in rotating superfluid or Bose-Einstein condensate which appears to be closely relevant to the Taylor-Proudman limit of compressible flows, the latter being responsible for a particular horizontally-incompressible

RSF [6]. For the less-known quantum Navier-Stokes, see, *e.g.*, most recently, J. W. Dong and Q. C. Ju, Blow-up of smooth solutions to compressible quantum Navier-Stokes equations, Sci Sin Math 50 (2020) 873–884; B. L. Guo and B. Q. Xie, Global existence of weak solutions to the three-dimensional full compressible quantum equations, Ann. of Appl. Math. 34 (2018) 1–31; J. W. Yang, G. H. Peng, H. Y. Hao and F. Z. Que, Existence of global weak solution for quantum Navier-Stokes system, International Journal of Mathematics 31 (2020), 2050038; and references therein.

[36] H. Ren and J.-Z. Zhu, "Statistical topological fluid mechanics: kinetic and dynamic studies of flows with real Schur form velocity gradients." 10th National Conference of Fluid Mechanics. Hangzhou, Zhejiang, China (2018).

[37] J.-Z. Zhu, Vorticity and helicity decompositions and dynamics with real Schur form of the velocity gradient, Phys. Fluids 30 (2018) 031703.